# A dynamic flotation model for predictive control incorporating froth physics. Part I: Model development

Paulina Quintanilla[a,*], Stephen J. Neethling[a], Daniel Navia[b], Pablo R. Brito-Parada[a]

[a] *Department of Earth Science and Engineering, Royal School of Mines, Imperial College London, South Kensington Campus, London SW7 2AZ, United Kingdom*
[b] *Departamento de Ingeniería Química y Ambiental, Universidad Técnica Federico Santa María, Campus San Joaquín, Santiago, Chile*

**Abstract**

It is widely accepted that the implementation of model-based predictive controllers (MPC) ensures optimal operation if an accurate model of the process is available. In the case of froth flotation, modelling for control purposes is a challenging task due to inherent process instabilities. Most models for control have only focused on the pulp phase rather than the froth phase, which is usually oversimplified or even neglected. Despite the fact that froth stability can significantly affect the overall performance of flotation cells, there is still a gap in literature regarding flotation models for control purposes that properly include froth physics.

In this paper we describe the development of a dynamic flotation model suitable for model predictive control, incorporating equations that describe the physics of flotation froths. Unlike other flotation models for control in the literature, the model proposed here includes important variables related to froth stability, such as bursting rate and air recovery, as well as simplified equations to calculate froth recovery and entrainment. These model equations allow estimating the amount of valuable material reporting to the concentrate, which can be used as a proxy to estimate grade and recovery. Additionally, pulp-froth interface physics was also included in our model, which enables a more accurate prediction of relevant flotation variables.

A sensitivity analysis of the parameters showed that two out of seven parameters were highly sensitive. The highly sensitive parameters are the exponential factor $n$ of the equation for the overflowing bubble size, and the constant value $a$ of the equation for the bursting rate. Although the other parameters showed a reasonably lower sensitivity than $n$ and $a$, the results also revealed that there is a significant difference in the prediction accuracy if the parameters are poorly estimated. Further simulations of important variables for control exhibited a good adaptability to changes in typical variables, such as air and feed flowrates.

An analysis of degrees of freedom of the model established that two variables need to be fixed to have a completely determined system. This means that two variables are available for control purposes, which can be air and tailings flowrates (through the manipulation of the respective control valves). This study therefore paves the way for the implementation of a robust dynamic model for flotation predictive control, incorporating important froth phenomena.

*Keywords:* Froth flotation, flotation modelling, flotation control, flotation simulations, model predictive

control, sensitivity analysis

## 1. Introduction

Control and optimisation of the froth flotation process have generated considerable research interest as even small improvements in the separation efficiency translate into important increments in production (Ferreira and Loveday, 2000; Maldonado et al., 2007; Jovanović and Miljanović, 2015; Quintanilla et al., 2021). Numerous investigations have established that one of the most efficient advanced control strategies to optimise a multivariable process is Model Predictive Control (MPC). However, the implementation of MPC in froth flotation still remains a challenge as it strongly relies on a dynamic model of the process that accurately predicts the future behaviour of the system (Desbiens et al., 1994, 1998; Bouchard et al., 2009; Sbarbaro and del Villar, 2010; Bergh and Yianatos, 2011; Shean and Cilliers, 2011; Quintanilla et al., 2021). The challenge comes from the lack of reliable, simplified (yet fundamentally-based) models that are capable of representing the froth flotation process as a whole. Most studies on flotation control have focused on model equations for the pulp phase, ignoring or simplifying the phenomena in the froth phase (Oosthuizen et al., 2017; Quintanilla et al., 2021). However, modelling the froth phase for this purpose is crucial as it defines the amount of material that reports to the concentrate (Neethling and Brito-Parada, 2018). This means that metallurgical indicators, such as recovery and grade, can be improved by implementing adequate models of the froth phase into advanced control strategies.

Although a number of dynamic, complex models for the froth phase have been developed for analysis purposes, such as those found in Varbanov et al. (1993); Neethling et al. (2003); Herbst and Harris (2007); Alves dos Santos et al. (2014); Jovanović et al. (2015); Wang et al. (2015); Gharai and Venugopal (2016); Dinariev and Evseev (2018); Prakash et al. (2018); Wang et al. (2018), a direct incorporation of such detailed models in control strategies is not feasible. The reason is that the model equations for control purposes must be simple enough – yet robust – to solve the control problem in real-time. Both characteristics conflict with each other; it is thus necessary to find a trade-off between simplicity and robustness.

Models for flotation control can be classified as empirical, phenomenological and hybrid models, from which model equations of the froth and pulp phase can be found. While an extensive literature review on modelling for flotation control purposes can be found in Quintanilla et al. (2021), here we focus the discussion on studies that have included froth phase models in their control strategy, in line with the main focus of this paper.

Bascur (1982) proposed semi-empirical model equations to determine the rate constant of the attachment and detachment sub-processes in the froth phase. These model equations were developed as a function of

*Corresponding author
*Email address:* p.quintanilla18@imperial.ac.uk (Paulina Quintanilla)

operating conditions such as the volumetric air flowrate ($Q_{air}$), particle size ($d_p$), bubble size in the froth ($d_{b,froth}$), froth depth ($h_f$), as well as linear ($\kappa_j^{FAT}$ and $\kappa_j^{FDT}$) and exponential ($n_c$) fitting parameters, as shown in Eqs. (1) and (2), respectively.

$$K_{ij}^{FAT} = \kappa_i^{FAT} Q_{air} \left(\frac{d_p}{d_{b,froth}}\right)\left(\frac{h_f}{d_{BF}}\right), \tag{1}$$

$$K_{ij}^{FDT} = \kappa_i^{FDT} \rho_i d_P^{n_c} u_\infty. \tag{2}$$

The term $\rho_j$ denoted the specific gravity of mineralogical class $i$, and $u_\infty$ is the bulk fluid velocity due to drainage. From the same study, the concentrate flowrate was also estimated by using the empirical equation presented in Eq. 3:

$$Q_C = a_c l_{lip} \left(h_f - h_T\right)^{1.5} \left(1 - \varepsilon_g, \right) \tag{3}$$

where $a_c$ is a fitting parameter, $l_{lip}$ is the overflowing lip length of the cell, $h_f$ is the froth depth, $h_T$ is the total flotation cell height. It is important to note, however, that a number of complex inter-related behaviours occur int he froth phase, empirical equations alone are insufficient to accurately represent it. Phenomenological models, therefore, must be used for robust modelling of the froth phase.

Phenomenological models for flotation control for the froth phase have been presented in Zaragoza and Herbst (1989); Putz and Cipriano (2015); Tian et al. (2018). For example, Zaragoza and Herbst (1989) described a kinetic model for the solid mass ($M_f$) in the froth phase, defined in terms of operating conditions including the concentrate flowrate ($Q_{conc}$), tailings flowrate ($Q_{tailings}$), the entrainment water flowrate ($Q_E$), and the air flowrate ($Q_{air}$):

$$\begin{aligned}\frac{dM_f}{dt} = &- \left(Q_R K_R + Q_{conc}\left(1+\alpha_f\right)\right) \frac{M_f}{\left(1+\alpha_f\right) V_{LF}} \\ &+ \left(Q_{tailings} + Q_{air}\frac{1-\varepsilon_g}{\varepsilon_g}\alpha_p\right) \frac{M_p}{\left(1+\alpha_p\right) V_{LP}}.\end{aligned} \tag{4}$$

The terms $\alpha_p$ and $\alpha_f$ in Eq. 4 are the equilibrium constants between the attachment and detachment in the pulp and froth phases, respectively. $\varepsilon_g$ is the gas hold-up, $V_{LP}$ is the volume of the liquid in the pulp, $V_{LF}$ is the volume of the liquid in the froth, $Q_R$ is the water flowrate draining back, and $K_R$ is a froth stability constant, which was not further explained by Zaragoza and Herbst (1989).

A similar approach was developed by Putz and Cipriano (2015). In their study, a phenomenological kinetic model was used to represented the mass transfer in the froth taking into consideration the attachment and detachment processes:

$$\frac{dM_f^{ijk}}{dt} = K_P^{ijk} M_P^{ijk} - \left[K_e^{ijk} + \frac{Q_C^i}{V_F^i}\right] M_f^{ijk}, \tag{5}$$

where $M_p^{ijk}$ is the mass of solids in the pulp phase and $M_f^{ijk}$ is the mass of solids in the froth phase, $Q_C^i$ is the concentrate volumetric flowrate, $K_e^{ijk}$ and $K_p^{ijk}$ are the flotation rates constants in the froth and pulp phases, respectively, $V_F^i$ are the pulp and froth volume of the cell $i$.

Another approach for modelling the froth phase using kinetic models was presented in Tian et al. (2018). While the model equations presented in Zaragoza and Herbst (1989) and Putz and Cipriano (2015) were developed for a flotation cell system, Tian et al. (2018) presented a froth phase model for control of a flotation column. The model equation used to represent the froth phase was a partial differential equation, shown in Eq. 6. One of the assumptions for Eq. 6 is that the froth phase is not mixed in the flow direction, but it is perfectly mixed in the direction perpendicular to the flow. This assumption, however, ignores the substantial vertical mixing that might occur in a flotation column.

$$\frac{\partial\left(\varepsilon_g C_a^F(z,t)\right)}{\partial t} = -\frac{\partial\left(U_a C_a^F(z,t)\right)}{\partial z} + \alpha_1 A v f C_{w_d}(z,t) + \sigma_1 A v f C_{w_u}(z,t) - \beta C_a^F(z,t). \tag{6}$$

The term $\varepsilon_g$ refers to the gas hold-up, $C_a^F$ is the mass concentration of solids particles in the air phase, $U_a$ is the velocity of particles within the air phase. $\alpha_1 A_v f C_{w_d}$ represents the transfer of particles from the downward water flow to the bubble; the term $\sigma_1 A_v f C_{w_u}$ represents the transfer of particles from the upward water flow to the babble; and the term $\beta C_a^F$ represents the particles detachment from the bubble. The initial conditions for the collection zone models were $C_a(0) = C_{a0}$, and $C_w(0) = C_{w0}$.

It can be noted that there are several limitations in the model presented in Tian et al. (2018). For example, the froth height, air hold-up, air flowrate, and attachment and detachment rates were considered as constants. This assumption is far from optimal as changes in operating variables such as the air flowrate, for instance, can have a very large impact on the operating conditions such as froth height and air hold-up.

The need to incorporate froth physics into control strategies is crucial as froth stability has a significant impact on the overall performance of flotation cells (Neethling and Brito-Parada, 2018). Air recovery has been used to measure froth stability in previous studies (Hadler and Cilliers, 2009; Hadler et al., 2010, 2012; Shean et al., 2017; Neethling and Brito-Parada, 2018). It is defined as the fraction of air entering the cell that does not burst (Neethling and Cilliers, 2008; Hadler and Cilliers, 2009; Hadler et al., 2010). Recent work by Oosthuizen et al. (2021) has considered froth physics in predictive control; the authors described a dynamic flotation model that combines fundamental mass and volume balances, steady-state froth models and empirical equations. Air recovery of each flotation cell $j$, $\alpha_j$, was modelled as a state variable, as follows:

$$\frac{d}{dt}\alpha_j = \frac{K_{\alpha_{BF}} D_{BF_j} + K_{\alpha_{jg}} j_{g_j} - \alpha_j}{\tau_{f_j}}. \tag{7}$$

The terms $K_{\alpha_{BF}}$, and $K_{\alpha_{j_g}}$ are empirical parameters to be calibrated; $j_g$ is the superficial gas velocity, and $\tau_f$ is the froth residence time. While it has been widely accepted that air recovery is measured by means of other variables (as shown below in Section 2, Eqs. 39 and 42), the derivation of the equation presented by

Oosthuizen et al. (2021) (Eq. 7) is not described in detail, nor is the model validated against air recovery data.

Another state variable defined in the aforementioned study was the froth bubble size of each flotation cell $j$, $D_{BF_j}$, as follows:

$$\frac{d}{dt}D_{BF_j} = \frac{K_{BS_{j_g}} j_{g_j} + K_{BS_{\tau_f}} \tau_{f_j} - D_{BF_j}}{\tau_{f_j}}, \tag{8}$$

where $K_{BS_{j_g}}$, $K_{BS_{\tau_f}}$ are empirical parameters to be calibrated. It was concluded that both states, $\alpha_j$ and $D_{BF_j}$, can be controlled by manipulating the superficial gas velocity ($j_g$), froth depth ($h_f$), tailings flowrate ($Q_{tailings}$) and the concentrate launder flowrate ($Q_H$). It was suggested that the process can be controlled at an optimum air recovery while maintaining a desired grade. However, this statement should be re-examined as concentrate grade is strongly associated with froth recovery, which was not explicitly included in this work. In fact, their study did not distinguish the difference between air recovery and froth recovery, as both variables were used as if they represented the same concept – which is a questionable assumption.

The pulp-froth interface plays a crucial role in froth stability as most of the detachment of solids particles occur in this region (Ata, 2012), significantly affecting the mineral recovery and grade (Chipili and Bhondayi, 2021). However, the inclusion of the interface in models for flotation control is yet another gap in the literature. Some attempts have been made by including, for example, the mass transfer between the froth and pulp phase by means of a constant rate for attachment and detachment of solids in the froth and pulp phases. These models have been discussed by Bascur (1982); Feteris et al. (1987); Herbst and Harris (2007); Herbst and Flintoff (2012); Jovanović et al. (2015), and implemented into control strategies by Zaragoza and Herbst (1989). This type of model, however, only considers the froth-pulp solid transfer rather than the physics of the interface itself. Besides, it does not include aspects related to the gas and liquid phases, such as changes in the upcoming gas velocity from the pulp phase, nor changes in bubble size. These changes in gas velocity and bubble size, in turn, play an important role in the prediction of froth stability.

Typically, the model equations presented in the studies mentioned above are oversimplified and insufficient to represent the froth phase. In fact, while an approach based on kinetics can be adequate to describe the phenomena in the pulp phase, the froth phase is dominated by more complex phenomena – such as bubble coalescence, liquid motion, and solid motion (Neethling et al., 2003). These phenomena cannot be modelled by kinetic or empirical equations, such as those used in the aforementioned studies. Although the most recent approach by Oosthuizen et al. (2021) on modelling the froth phase for control seems to be more promising to incorporate froth physics into predictive control; it still lacks of model equations that link froth stability to the overall flotation performance, such as the inclusion of bubble coalescence and bursting rate in the model (Neethling and Brito-Parada, 2018).

Therefore, in this study we propose a dynamic flotation model, for a potential implementation of MPC,

that incorporates the froth phase physics. This study is presented as a two-part paper. In this fist part, the model development, sensitivity analysis of the parameters, and simulations of important variables for control are presented. The model calibration and validation, performed using experimental data obtained from an 87-litre laboratory scale flotation tank, are presented in Part II. Selected data obtained from these experiments were also used for the sensitivity analysis and simulations presented in this manuscript.

## 2. Model development

For ease of explanation, the equations in our model have been classified as equations for the conservation of mass (Section 2.1), the pulp phase (Section 2.2), the interface (Section 2.3), and the froth phase (Section 2.4). However, the implementation of the complete model follows a different path, since it is a High Index DAE (Differential and Algebraic Equations) system. In the Appendix, Table 5 presents the nomenclature used in this section, along with the units of each variable, while Table 6 summarises the model equations of each phase, along with their classification (phenomenological/semi-empirical/empirical).

The proposed mathematical model was developed considering the flotation cell as a well-mixed, continuous stirred tank reactor (CSTR) in the pulp phase. It was also assumed that the feed flowrate, head grade, fraction of solids and bubble size classes in the pulp, particle sizes for the different species, and solids density were known beforehand.

### *2.1. Conservation of mass for each mineralogical species i*

To begin with the model development for a single flotation cell, we firstly define an overall mass balance as shown in Eq. 9. These equations include the change in the concentration of particles that belong to a mineralogical class $i$.

$$\frac{dM_i}{dt} = m_{i,feed} - m_{i,tailings} - m_{i,TF} - m_{i,ENT}. \tag{9}$$

The term $\frac{dM_i}{dt}$ represents the rate change of mass of the mineralogical class $i$, which is calculated considering those particles entering into the flotation cell in the feed ($m_{i,feed}$), and leaving the cell in the tailings ($m_{i,tailings}$) and in the concentrate ($m_{i,TF}$ and $m_{i,ENT}$). The terms $m_{i,TF}$ and $m_{i,ENT}$ denote the mass of particles of mineralogical class $i$ that report to the concentrate due to true flotation (TF) and entrainment (ENT), respectively.

### *2.2. Pulp phase model*

Pulp phase model equations have been widely developed for control purposes (Quintanilla et al., 2021). The model equations used in this work to calculate the solid mass flowrate in the feed ($m_{i,feed}$) and in the tailings ($m_{i,tailings}$) are presented below.

**Solid mass flowrate in the feed -** The term $m_{i,feed}$ represents the solid mass flowrate in the feed for each mineralogical class $i$. This term depends on the mass fraction of the mineral, $C_{i,f}$, and the volumetric flowrate in the feed, as shown in Eq. 10. Here, it was assumed that the head grade and the mineral species were known beforehand, and therefore $C_{i,f}$ can be calculated using this information.

$$m_{i,feed} = C_{i,f} Q_{feed} \tag{10}$$

The volumetric flowrate of the feed, $Q_{feed}$, is assumed to be measured on-line and, therefore, it has a known value. This is a valid assumption given that $Q_{feed}$ is typically measured on plant because it is needed to calculate the metallurgical recovery. In case $Q_{feed}$ were not available, it can be estimated using, for example, moving horizon estimation (MHE) or control vector parameterization (CVP). In Part II of this study, CVP was used to estimate $Q_{feed}$ for model validation purposes.

**Solid mass flowrate in the tailings -** The term $m_{i,tailings}$ denotes the solid mass flowrate in the tailings for each mineralogical class $i$, which can be calculated using Eq. 11.

$$m_{i,tailings} = C_{i,tailings} Q_{tailings}, \tag{11}$$

where $C_{i,tailings}$ is the mass concentration of solids in the tailings, and $Q_{tailings}$ is the tailings flowrate that is assumed to be known from the regulatory control system. In terms of modelling, the tailings flowrate can be also estimated as described in Eq. 12, assuming that the valve constant ($K_v$), control signal ($u_v$), pulp height ($h_p$) and gas hold-up in the pulp ($\varepsilon_0$) are measured or estimated. It must be noted that the pulp height and gas hold-up can be calculated as shown later in Eq. 21 and 17, respectively.

$$Q_{tailings} = K_v u_v \sqrt{h_p(1-\varepsilon_0)}, \tag{12}$$

Assuming that the flotation cell behaves as a CSTR, the concentration of particles in the tailings for each mineralogical class is:

$$C_{i,tailings} = \frac{M_i}{V_{pulp}}. \tag{13}$$

The mass of each mineralogical class $M_i$ is calculated from Eq. 9. The term $V_{pulp}$ corresponds to the total pulp volume in the cell. This volume is given by the sum of liquid volume ($h_0 A_{cell}$) and gas volume ($V_{gas}$):

$$V_{pulp} = h_0 A_{cell} + V_{gas}, \tag{14}$$

where $h_0$ is the "gas free" height, i.e. only liquid (from Eq. 19), and $A_{cell}$ is the cross-sectional area of the flotation cell. The gas volume ($V_{gas}$) is calculated as the contribution of the volume of each bubble size $k$:

$$V_{gas} = \sum_{k=1}^{K} V_{gas}^{k}. \tag{15}$$

The gas volume of each bubble size class ($V_{gas}^{k}$) is given by:

$$V_{gas}^{k} = \frac{\varepsilon_0^k}{1-\varepsilon_0^k} h_0 A_{cell}, \tag{16}$$

where $\varepsilon_0^k$ is the gas hold-up for each bubble size class $k$, which is calculated using Eq. 17. A detailed derivation of Eq. 17 can be found in (Shean et al., 2018).

$$\frac{d\left(\frac{\varepsilon_0^k}{1-\varepsilon_{0,\text{total}}}\right)}{dt} = \frac{1}{h_0}\left(\frac{Q_{\text{air},in}^k}{A} - v_{\text{g,out pulp}}^k \varepsilon_0^k\right) - \frac{1}{h_0}\left(\frac{Q_{\text{feed}}}{A_{\text{cell}}} - \frac{Q_{\text{pulp,out}}}{A_{\text{cell}}}\right)\left(\frac{\varepsilon_0^k}{1-\varepsilon_{0,\text{total}}}\right). \tag{17}$$

The term $\varepsilon_{0,total}$ denotes the total gas hold-up in the pulp phase, and $v_{g,\text{out pulp}}^k$ is the upward gas velocity out of the pulp from Eq. 32. The total gas hold-up ($\varepsilon_{0,total}$) is the sum of each bubble size class $k$:

$$\varepsilon_{0,\text{total}} = \sum_{k=1}^{K} \varepsilon_0^k. \tag{18}$$

The gas free pulp height ($h_0$) is derived from a material balance in the cell as (Shean et al., 2018):

$$\frac{dh_0}{dt} = \frac{Q_{feed}}{A_{cell}} - \frac{Q_{pulp,out}}{A_{cell}}, \tag{19}$$

where $Q_{\text{pulp, out}}$ is the sum of both overflows from the flotation cell:

$$Q_{\text{pulp,out}} = Q_{\text{tailings}} + Q_{\text{conc}}. \tag{20}$$

The total pulp height ($h_p$), which considers the contribution from the liquid and gas phases in the pulp, is defined as (Shean et al., 2018):

$$h_p = \frac{h_0}{1-\varepsilon_{0,\text{ total}}}, \tag{21}$$

where $h_0$ is the gas free height calculated from Eq. 19 and $\varepsilon_{0,total}$ is the total gas hold-up in the pulp from Eq. 18. It must be noted that here we need to solve the high index problem to determine $h_p$. To do so, the derivative of pulp height in time from Eq. 21 is calculated by applying the chain rule:

$$\frac{dh_p}{dt} = \frac{1}{A_{cell}}\left(Q_{feed} - Q_{pulp,out}\right)\left(\frac{1}{1-\sum_{k=1}^{K}\varepsilon_0^k}\right) + \frac{h_0}{\left(1-\sum_{k=1}^{K}\varepsilon_0^k\right)}\sum_{k=1}^{K}\frac{d\varepsilon_0^k}{dt}. \tag{22}$$

From Eq. 17 we can obtain an expression to calculate $\frac{d\varepsilon_0^k}{dt}$, which has a matrix form as below:

$$Ax = B, \tag{23}$$

where $x$ represents the rate change of gas hold-up ($\varepsilon_0$):

$$x = \frac{d\varepsilon_0^k}{dt}. \tag{24}$$

The matrices $A$ and $B$ correspond to:

$$A = \begin{bmatrix} b_1 & a_1 & \cdots & \cdots & \cdots & a_1 \\ a_2 & b_2 & \cdots & \cdots & \cdots & a_2 \\ a_3 & a_3 & b_3 & \cdots & \cdots & a_3 \\ \vdots & \vdots & \vdots & \ddots & \cdots & \vdots \\ \vdots & \vdots & \vdots & \cdots & \ddots & \vdots \\ a_K & \cdots & \cdots & \cdots & \cdots & b_K \end{bmatrix}, \tag{25}$$

$$a_k = \frac{\varepsilon_0^k}{\left(1 - \sum_{k=1}^{K} \varepsilon_0^k\right)^2}, \tag{26}$$

$$b_k = a_k + \frac{1}{\left(1 - \sum_{k=1}^{K} \varepsilon_0^k\right)}, \tag{27}$$

and:

$$B = \begin{bmatrix} B_1 \\ \vdots \\ B_K \end{bmatrix}, \tag{28}$$

where:

$$B_k = \frac{1}{h_0}\left(\frac{Q_{air,in}^k}{A} - v_{g,outpulp}^k \varepsilon_0^k\right) - \frac{1}{h_0}\left(\frac{Q_{\text{feed}}}{A_{\text{cell}}} - \frac{Q_{\text{pulp,out}}}{A_{\text{cell}}}\right)\left(\frac{\varepsilon_0^k}{1 - \sum_{k=1}^{K} \varepsilon_0^k}\right). \tag{29}$$

The term $Q_{air,in}^k$ is calculated as the total air flowrate entering into the cell ($Q_{air,in}$) multiplied by the proportion of each bubble size class $k$:

$$Q_{air,in}^k = Q_{air,in} \Psi_{d_{b,pulp}}^k, \tag{30}$$

where $\psi_{d_{b,pulp}}$ is the proportion of each bubble size class in the pulp phase ($k$) calculated from data of bubble size distribution. For example, if a bubble sizer is available on site, it is possible to measure the distribution of bubble sizes in the pulp, as explained in Morrison et al. (2017); Mesa and Brito-Parada (2020). From

that distribution, a number of bubble size classes $K$ must be chosen, and then the proportion of each bubble size class is calculated using the frequency of each class, as follows:

$$\Psi^{k}_{d_{b,pulp}} = \frac{(\text{frequency bubble size class})_k}{\sum_{k=1}^{K}(\text{frequency bubble size class})_k}. \tag{31}$$

While Eqs. (23-29) allow calculating the rate of change of gas hold-up in the pulp phase for any number of bubble size classes $K$, it must be noted that the resolution time will be considerably higher when considering a high $K$. In this study, we considered 5 bubble size classes that were obtained by measuring bubble sizes in the pulp using a bubble viewer as described in Tucker et al. (1994); Chen et al. (2001); Grau and Heiskanen (2002); Mesa and Brito-Parada (2020). The value of the chosen $K$ comes from a parametric analysis and simulations in which different number of $K$ were considered. From the analysis, it was noted that $K = 5$ was sufficient to have an adequate accuracy against experimental data, as well as a significantly short elapsed time for the simulations. A sensitivity analysis is presented in Section 3.1, and a further discussion on choosing $K$ is made in the model validation section, in Part II of this paper.

To solve the equation for gas hold-up, it is necessary to calculate the upward gas velocity out of the pulp ($v^{k}_{g,\text{out pulp}}$), which can be estimated as (Coulson and Richardson, 1993; Ityokumbul et al., 1995; Shean et al., 2018):

$$v^{k}_{g,\text{out pulp}} = \frac{g\rho_{\text{pulp}}(d^{k}_{b,pulp})^2}{18\mu_{\text{pulp}}\left(1-\varepsilon^{k}_{0}\right)^{1.39}}, \tag{32}$$

where $g$ is gravity force assumed equal to 9.81 $\frac{m}{s^2}$, $\rho_{pulp}$ and $\mu_{pulp}$ are the density and viscosity of the pulp, respectively, and $d^{k}_{b,pulp}$ is the bubble size class $k$. The total gas velocity out of the pulp ($v^{total}_{g,\text{out pulp}}$) is the weighted sum of the velocity of each bubble size, which is calculated as:

$$v^{\text{total}}_{g,\text{out pulp}} = \sum_{k=1}^{K} v^{k}_{g,\text{out pulp}}\varepsilon^{k}_{0}. \tag{33}$$

The density of the pulp can be assumed constant (Shean et al., 2018), and it is calculated as a function of the solid density and the volumetric fraction of solids, $\phi$, as below:

$$\rho_{\text{pulp}} = \phi\rho_{\text{sol}} + (1-\phi)\rho_{\text{water}}. \tag{34}$$

The term $\phi$ refers to the volumetric fraction of solids, which can be calculated in terms of the densities and the total mass fraction of solids, $\Phi_{solids}$, as:

$$\phi = \frac{\rho_{\text{water}}}{\rho_{\text{water}} - \rho_{\text{solids}} + \frac{\rho_{\text{solids}}}{\Phi_{solids}}}. \tag{35}$$

The pulp viscosity, $\mu_{pulp}$, used in Eq. 32 can be calculated using the water viscosity ($\mu_{water}$) and the volumetric fraction of solids ($\phi$) as:

$$\mu_{\text{pulp}} = \mu_{\text{water}} \exp\left(\frac{2.5\phi}{1 - 0.609\phi}\right). \tag{36}$$

.

### *2.3. Pulp-froth interface model*

Model equations for the pulp-froth interface are also required in order to obtain a complete flotation model. As mentioned in the Introduction, the interface is typically neglected for control purposes. The equations presented here, thus, provide a significant, novel contribution to the field of modelling for flotation control as they allow a more accurate prediction of relevant flotation variables.

At the interface, the gas velocity is different from that in the pulp phase, as it is also influenced by the changes in pulp height. In Eq. 37 the interfacial gas velocity ($v_g^*$) is presented as the contribution of the velocity of each bubble size $v^{total}_{g,\text{out pulp}}$, and the change in pulp height with time, ($\frac{dh_p}{dt}$).

$$v_g^* = \frac{dh_p}{dt} + v^{\text{total}}_{g,\text{ out pulp}}. \tag{37}$$

It can be noted that the first term represents the rate of change in pulp height, which can be calculated from Eq. 22. The second term is the total gas velocity out of the pulp from Eq. 33.

Another important interface variable, which will be used to calculate froth recovery (Eq. 54) and the overflowing bubble size at the lip cell (Eq. 47), is the mean bubble size at the interface ($d_{b,int}$). This term is calculated as shown in Eq. 38, where $v^k_{gas,\text{out pulp}}$ is calculated from Eq. 32, $\varepsilon_0^k$ is calculated from Eq. 17, and $d^k_{b,pulp}$ is the bubble size in the pulp phase of class $k$.

$$d_{b,int} = \frac{\sum_{k=1}^{K} v^k_{gas,\text{out pulp}} \varepsilon_0^k}{\sum_{k=1}^{K} \frac{v^k_{gas,\text{out pulp}} \varepsilon_0^k}{d^k_{b,pulp}}}. \tag{38}$$

### *2.4. Froth phase model*

A phenomenological simplified model of the froth phase for control purposes is presented in this sub-section. Model equations to calculate the last two terms ($m_{i,TF}$ and $m_{i,ENT}$) of the conservation of mass shown in Eq. 9 are also described below.

Most of the model equations for the froth phase are dependant upon air recovery, $\alpha$. Air recovery is defined as the fraction of air that overflows but do not burst (Neethling and Cilliers, 2008; Hadler and Cilliers, 2009; Hadler et al., 2010). There are a number of studies that discuss the importance of air recovery on flotation performance (Hadler and Cilliers, 2009; Hadler et al., 2010; Shean et al., 2017; Neethling and Brito-Parada, 2018), as it is a measure of froth stability. It has been shown that air recovery passes through a peak as the

air flowrate increases. It has been demonstrated by Hadler and Cilliers (2009) that a Peak in Air Recovery (PAR) indicates the air flowrate at which the highest mineral recovery is obtained. Air recovery is calculated as shown in Eq. 39.

$$\alpha = \frac{v_f l_{lip} h_{over}}{Q_{air,in}}, \tag{39}$$

where $v_f$ is the overflowing velocity over the lip, $l_{lip}$ is the lip length, $h_{over}$ is the froth height and $Q_{air,in}$ is the air flowrate.

The overflowing froth velocity over the lip ($v_f$) can be measured online using image analysis. It can also be estimated using Eq. 40, which is as a function of concentrate flowrate (from Eq. 44), length of the lip of the cell ($l_{lip}$) and the slurry content in the froth $\epsilon$.

$$v_f = \frac{Q_{\text{concentrate}}}{\epsilon l_{\text{lip}}\ h_{\text{over}}}. \tag{40}$$

The slurry content ($\epsilon$), which refers of the volume of liquid and solids in the froth phase, is calculated using Eq. 41, assuming that the cross-sectional Plateau border area remains constant with froth depth and, therefore, has the same value at the level of the overflow lip. This results in (Neethling and Cilliers, 2008):

$$\epsilon \approx \begin{cases} \frac{v_g^*}{k_1}\left(1-\alpha^*\right)\lambda_{out} \text{ if } \alpha < 0.5 \\ \frac{v_g^*}{2k_1}\lambda_{\text{out}} \text{ if } \alpha \geq 0.5 \end{cases} \tag{41}$$

where $v_g^*$ is the interfacial gas velocity (from Eq. 37), $k_1$ is the physical parameter (from Eq. 45), and $\lambda_{out}$ is the length of Plateau border per volume of froth (from Eq. 46).

In order to incorporate froth stability measurements in the model, we have included the term $\alpha^*$ as the air recovery calculated with the actual rate at which bubbles burst at the surface of the froth (i.e. bursting rate ($v_b$)). A similar approach has been taken previously by Neethling and Brito-Parada (2018). The model equation for the term $\alpha^*$ is:

$$\alpha^* = \frac{v_g^* - v_b}{v_g^*}, \tag{42}$$

where $v_g^*$ is the interfacial gas velocity (from Eq. 37), and $v_b$ is the bursting rate at the top of the froth. The bursting rate at the top of the froth has been shown to have at least a second order relationship with superficial gas velocity ($j_g$) (Neethling and Brito-Parada, 2018), depending on the operating conditions in the flotation cell, to predict a peak in air recovery (PAR). The bursting rate is thus can be estimated as:

$$v_b = a + bj_g + cj_g^2, \tag{43}$$

where the superficial gas velocity is $j_g = Q_{air,in}/A_{cell}$. A sensitivity analysis of the parameters $a, b$ and $c$ is presented in Section 3.1. In this study, some variables in the froth phase model, such as the concentrate

flowrate, froth recovery, and entrainment factor, depend on the value of $\alpha^*$, and they change depending on whether $\alpha^*$ is lower or greater than 0.5.

The concentrate flowrate can be calculated as Eq. 44 from Neethling et al. (2003):

$$Q_{conc} = \begin{cases} \frac{A_{cell} v_g^{*2} \lambda_{out} (1-\alpha^*) \alpha^*}{k_1} & \text{if } \alpha < 0.5 \\ \frac{A_{cell} v_g^{*2} \lambda_{out}}{4 k_1} & \text{if } \alpha \geq 0.5 \end{cases}, \tag{44}$$

where $A_{cell}$ is the cell cross-sectional area, $v_g^*$ is the interfacial gas velocity (from Eq. 37), $\lambda_{out}$ is the length of the Plateau border, $\alpha^*$ is the froth air recovery, and $k_1$ is a physical parameter that is calculated as in Eq. 45:

$$k_1 = \frac{\rho_{\text{pulp}} g}{3 C_{PB} \mu_{\text{pulp}}}, \tag{45}$$

where $\rho_{pulp}$ is the pulp density from Eq. 34 and $\mu_{pulp}$ is the pulp density calculated from Eq. 36. The term $C_{PB}$ represents the drag coefficient that is assumed to be constant and equals to 50.

The length Plateau border out of the froth per volume of froth ($\lambda_{out}$) is calculated as shown in Eq. 46, where the bubbles are assumed to be Kelvin cells (i.e. $k_\lambda = 6.815$) (Neethling et al., 2003):

$$\lambda_{out} = \frac{k_\lambda}{d^2_{\text{bfroth out}}}. \tag{46}$$

The term $d_{b,\text{froth out}}$ denotes the bubble size at the lip cell, i.e. it can be considered as "overflowing bubble size". In order to estimate this variable, we have assumed that the rate of changes in bubble size in the froth takes the following form:

$$\frac{d}{dt} d_{b,froth} = C d_{b,froth}^{1-n}, \tag{47}$$

where $C$ and $n$ are parameters to be calibrated with experimental data, with $n$ having a value between 1 and 2 (Neethling and Cilliers, 2003). The obvious and easiest way to calibrate these parameters would be by measuring the overflowing bubble size. However, this is very difficult to implement in practice (Wang and Neethling, 2006) and, therefore, we have calibrated them using the water recovery from experimental data, as detailed in Part II of this paper. A sensitivity analysis of $n$ and $C$ is presented in Section 3.1. The analytical solution for $d_{b,\text{froth out}}$ is presented in Eq. 47. This solution was obtained by considering a volume control from the interface to the lip cell, and from $t = 0$ to $t = \tau_f$.

$$d_{\text{bfroth out}} = \left( n C \tau_f + d_{b,int}^n \right)^{1/n}, \tag{48}$$

where $d_{b,int}$ is the bubble size in the interface from Eq. 38. The term $\tau_f$ is the average residence time in the froth phase, which can be estimated as:

$$\tau_f = \frac{h_f}{v_g^*}, \tag{49}$$

where $h_f$ is the froth depth, and $v_g^*$ is the interfacial gas velocity from Eq. 37. The froth depth ($h_f$) can be approximated as:

$$h_f = h_T - h_p, \tag{50}$$

where $h_T$ is the total height of the flotation cell, and $h_p$ is the pulp height from Eq. 21.

**Solid transfer due to true flotation -** The third term of the conservation of mass in Eq. 9 is the mass of solids transferred to the froth due to true flotation ($m_{i,TF}$), which is calculated as:

$$m_{i,\text{true flotation}} = V_{\text{cell}} k_i R_{f,i} C_{\text{tailings},i}, \tag{51}$$

where $V_{cell}$ is the volume of the flotation cell, $k_i$ is the specific rate constant for the mineralogical specie $i$, $R_{f,i}$ is the froth recovery factor and $C_{tailings,i}$ is the mass concentration of the mineralogical specie $i$ (from Eq. 13). The specific rate constant ($k_i$) is defined as Eq. 52, as a function of the floatability of the mineralogical class $i$ ($P_i$) and the bubble surface area flux ($S_b$).

$$k_i = P_i S_b \tag{52}$$

The bubble surface area flux $S_b$ is obtained by means of Eq. 53, as a function of the interfacial gas velocity (from Eq. 37) and the interfacial bubble size (from Eq. 38).

$$S_b = \frac{6 v_g^*}{d_{b,int}} \tag{53}$$

The froth recovery factor in Eq. 51 is defined as the fraction of the material entering the froth attached to the bubbles that reports to the concentrate, rather than dropping back into the pulp (Finch and Dobby, 1991; Neethling and Cilliers, 2008). Although it is difficult to measure, it can be estimated using Eq. 54, which is a simple theoretical approximation developed in Neethling and Cilliers (2008).

$$R_{F,i} = \begin{cases} \left(\frac{\alpha^*(1-\alpha^*)v_g^*}{v_{\text{set},i}}\right)^{\frac{f}{2}} \left(\frac{d_{b,\text{ int}}}{d_{\text{bfroth}}}\right)^f & \text{if } \alpha < 0.5 \\ \left(\frac{v_g^*}{v_{\text{set},i}}\right)^{\frac{f}{2}} \left(\frac{d_{b,\text{ int}}}{d_{\text{bfroth}}}\right)^f & \text{if } \alpha \geq 0.5 \end{cases} \tag{54}$$

The term $f$ in Eq. 54 is a constant value between 0 and 1, and represents the fraction of material that becomes detached from the bubble surfaces during coalescence (Neethling and Cilliers, 2008; Hu et al., 2013).

Froth recovery also depends on the froth air recovery $\alpha^*$ (Eq. 42), the interfacial gas velocity $v_g^*$ (Eq. 37), the particle settling velocity $v_{set,i}$, the interfacial bubble size $d_{b,int}$ (Eq. 38), and the overflowing bubble size $d_{b,froth}$ (Eq. 47)).

The particle settling velocity $v_{set,i}$ is calculated as below:

$$v_{set,i} = \frac{g\left(\rho_{\text{solid},i} - \rho_{\text{water}}\right) d_{p,i}^2}{18\mu_{\text{pulp}}} \frac{(1-\phi)^{4.65}}{3}, \tag{55}$$

where $\rho_{solid,i}$ is the density of the solid of mineralogical class $i$, $\rho_{water}$ is the water density, $\mu_{pulp}$ is the pulp density (Eq. 36), and $\phi$ is the volumetric solid fraction (Eq. 35).

**Solid transfer due to entrainment -** The last term in Eq. 9 for the conservation of mass, $m_{i,ENT}$, corresponds to the transfer of mass of solids to the froth phase due to entrainment. This term is calculated using Eq. 56, which is a function of the entrainment factor ($ENT_i$). The entrainment factor refers to the proportionality between the amount of gangue entrained and the water recovery. Estimating entrainment is vital to predict flotation performance, as it is related to the concentrate grade.

$$m_{i,ENT} = Q_{\text{conc}} ENT_i C_{\text{tailings},i} \tag{56}$$

The term $Q_{conc}$ is the concentrate volumetric flowrate from Eq. 44, $ENT_i$ is the entrainment factor of the mineralogical specie $i$, and $C_{tailings,i}$ is the mass concentration of the mineralogical specie $i$ from Eq. 13. The entrainment factor can be calculated as shown in Eq. 57 (Neethling and Cilliers, 2009).

$$ENT_i \approx \begin{cases} \exp\left(\frac{-v_{set,i}^{1.5} h_f}{D_{axial}\sqrt{v_g^*(1-\alpha^*)}}\right) & \text{if } \alpha < 0.5 \\ \exp\left(\frac{-2v_{\text{set},i}^{1.5} h_f}{D_{\text{axial}}\sqrt{v_g^*}}\right) & \text{if } \alpha \geq 0.5 \end{cases} \tag{57}$$

In the above equations, $v_{set,i}$ is the particle settling velocity (from Eq. 55), $h_f$ is the froth depth (from Eq. 50), $D_{axial}$ is the axial dispersion, $v_g^*$ is the interfacial gas velocity (from Eq. 37), and $\alpha^*$ is the froth air recovery (from Eq. 42). The axial dispersion is calculated as below:

$$D_{\text{axial}} = \frac{j_g^{1.5}}{\sqrt{k_1\left(\sqrt{3} - \frac{\pi}{2}\right) Pe}}, \tag{58}$$

where $j_g$ is the superficial gas velocity, the term $k_1$ is the physical parameter (from Eq. 45), and $Pe$ is the Péclet number, which can be assumed constant and equals to 0.15 (Lee et al., 2005; Hu et al., 2013).

## 3. Results and discussion

In the previous section we presented a dynamic model that can be used in predictive control strategies. Unlike other models found in the literature, the model proposed here incorporates froth stability by including

crucial model equations, such as those presented for air recovery, bursting rate, and bubble coalescence. As discussed in the Introduction, the inclusion of the froth phase in models for predictive control is crucial as this phase defines the amount of valuables reported to the concentrate. In fact, including froth stability in the model allows a better estimation of metallurgical indicators, such as grade and recovery, which can be used as part of the control strategy.

Besides the incorporation of froth physics, the model proposed here also presents a number of other advantages over other models found in the literature. For example, our model is based in the phenomenology of the process, having only a few number of parameters to be estimated. This is particularly useful for predictive controllers as they have to be updated in real-time to obtain more accurate predictions. Additionally, the model also incorporates pulp-froth interface phenomenology, which enables greater accuracy in the model predictions.

An analysis of degrees of freedom has been conducted in order to further explore the effectiveness of implementation in control. The analysis of degrees of freedom reveals the maximum number of variables that need to be fixed to have a completely determined model (Rodríguez and Gayoso, 2006). Table 1 summarises the analysis of degree of freedom of the model presented in Section 2. The total number of variables $(29 + 12i + 5K)$ are shown in Table 5. A summary of the model equations is presented in Table 6, from which it can be seen that the model has a total of $26+10i+5K$ equations. The number of variables specified externally takes into account the feed flowrate ($Q_{feed}$), the grade in the feed for each mineralogical class ($C_{f,i}$) and the particle size ($d_{p,i}$).

Table 1: Analysis of degree of freedom. The term $i$ stands for the number of mineralogical classes, and $K$ is the number of bubble size classes in the pulp phase.

| | |
|---|---|
| Number of variables | $29 + 12i + 5K$ |
| Number of equations | $-(26 + 10i + 5K)$ |
| Number of variables specified externally | $-(1 + 2i)$ |
| **Degrees of freedom for control** | 2 |

Two degrees of freedom mean that two variables are available as manipulated variables for control. In this case, the most obvious ones are the tailings flowrate ($Q_{tailings}$) and the air flowrate entering into the cell ($Q_{air,in}$). Simulations were carried out for different operating conditions in order to assess the predictive ability of the model proposed.

In this section, we present simulations that were carried out to perform the sensitivity analysis of the parameters in the model, as well as to analyse important output variables. To do so, experimental data were used as input data for the simulations. The experimental data used were the feed flowrate ($Q_{feed}$), tailings flowrate ($Q_{tailings}$), bubble size in the pulp ($d_{b,pulp}$), and froth height over the cell lip ($h_f$). It should

be noted that these data do not affect the sensitivity analysis of the parameters as they do not influence directly the variables analysed here.

The dimensions of the flotation cell used for the simulation are presented in Table 2, which are the same as the experimental setup presented in Part II of this paper. Additionally, the properties of the feed flowrate used for the sensitivity analysis and simulations are presented in Table 3.

Table 2: Flotation cell dimensions used for the sensitivity analysis of the parameters of the model (Section 3.1) and for the simulations (3.2). These dimensions are the same as those of the experimental system used for experiments in Part II of this paper.

| **Flotation cell dimensions** | **Symbol** | **Value** | **Unit** |
|---|---|---|---|
| Cross-sectional area of the cell | $A_{cell}$ | 0.18 | $m^2$ |
| Volume of the cell | $V_{cell}$ | 0.087 | $m^3$ |
| Total height of the cell | $h_T$ | 0.48 | $m$ |
| Lip length | $l_{lip}$ | 1.51 | $m$ |

Table 3: Feed properties used for the sensitivity analysis of the parameters of the model (Section 3.1) and for the simulations (Section 3.2). These feed properties are the same as those used in the experiments performed for model calibration and validation in Part II of this paper.

| **Feed properties** | **Symbol** | **Value** | **Unit** | **Source** |
|---|---|---|---|---|
| Water density | $\rho_{water}$ | 1000 | $kgm^{-3}$ | Assumption |
| Water viscosity | $\mu_{water}$ | $10^{-3}$ | $Pa\ s$ | Assumption |
| Solids density | $\rho_{solids}$ | 2500 | $kgm^{-3}$ | Supplied by manufacturer |
| Gravity | $g$ | 9.81 | $ms^{-2}$ | Assumption |
| Particle size | $d_{P,i}$ | $75 \times 10^{-6}$ | $m$ | Supplied by manufacturer |
| Solid fraction | $\Phi$ | 0.2 | - | Experimental setup |

### *3.1. Sensitivity analysis of fitting parameters*

The fitting parameters of the model proposed in Section 2 are: $n$ and $C$ from Eq. 47; $a$, $b$ and $c$ from Eq. 43; $f$ from Eq. 54; and the number of bubble size classes $K$ from Eqs. 16, 17, 30, 31, and 32. A sensitivity analysis for all of these fitting parameters was performed, which allowed comparing the changes with respect to a nominal value for both the variables and the parameter. The nominal values are presented in Table 4.

Table 4: Nominal values for the fitting parameters of the model to assess their sensitivity. The variables of the model affected by these parameters, as well as the corresponding equations are also presented in the table.

| **Fitting parameter** | **Nominal value** | **Units** | **Variable(s)** | **Equation(s)** |
|---|---|---|---|---|
| n | 1.5 | - | $d_{\text{b, froth out}}$, $Q_{conc}$ | 44 and 47 |
| C | $1.00 \times 10^{-5}$ | – | $d_{\text{b, froth out}}$, $Q_{conc}$ | 44 and 47 |
| a | 0.00339 | $m\ s^{-1}$ | $v_b$ | 43 |
| b | 0.0012 | - | $v_b$ | 43 |
| c | 24.6 | - | $v_b$ | 43 |
| K | 5 | - | $V^k_{gas}$,$\varepsilon^k_0$, $Q^k_{air,in}$, $\Psi^k_{d_b,pulp}$, $v^k_{g,\text{out pulp}}$ | 16, 17, 30, 31, 32 |
| f | 0.5 | - | $R_f$ | 54 |

The sensitivity analysis was performed by varying only the fitting parameter to be analysed whilst the rest are maintained constant at their nominal value (Table 4). Besides, all other inputs in the model, such as those shown in Table 2 and 3, as well as input variables such as $j_g$, $Q_{feed}$ and $Q_{tailings}$, were also maintained constant.

A transient analysis was performed for the fitting parameters $n$, $C$, $f$ and $K$, while the analysis for $a$, $b$ and $c$ from the bursting rate equation was performed at steady-state. The reason for the steady-state analysis is that the bursting rate equation only depends on $j_g$, which has a very rapid dynamics; hence, the analysis did not change over time.

*3.1.1. Fitting parameters n and C (Eq. 47):*

A sensitivity analysis was carried out for the fitting parameters $n$ and $C$ from Eq. 47 at dynamic state as $d_{d,\text{froth, out}}$ depends on dynamic variables (residence time in the froth, $\tau_f$, and bubble size in the interface, $d_{b,int}$). In this case, the overflowing bubble size ($d_{b,\text{out pulp}}$) was analysed as it is directly affected by these parameters. The effect of these fitting parameters on the concentrate flowrate ($Q_{conc}$) of Eq. 44 was also analysed, as it depends on $\lambda_{out}$ (Eq. 46), which is inverse to the square of the overflowing bubble size and, thus, depends on $n$ and $C$ as well. It should be noted that the concentrate flowrate is an important variable to take into consideration as it determines the water recovery, which is strongly related to the gangue recovery in the concentrate.

The fitting parameter $n$ could only be changed between ±30% with respect to its nominal value of 1.5, since it would otherwise be out of its feasible range (between 1 and 2). Figure 1 shows the changes in the dynamic overflowing bubble size with respect to variations in the $n$ value. It can be seen that $d_{b,\text{froth out}}$ has a major impact when $n$ has variations between 10 to 30 % from its nominal value, i.e. for values of $n$ approaching 2. While overflowing bubble size variations for positive changes of $n$ range from 100 to 300 %, smaller variation are obtained for negative changes of $n$, obtaining variation up to $-80\%$ in $d_{b,\text{froth out}}$. It can be also seen

in the box plot in the right that there is a clear trend of decreasing the dispersion of the variation of the overflowing bubble size as the $n$ value approaches 1, since the dynamic responses for this range are flatter. This is in some sense expected as the parameter $n$ is located in the exponential expression in Eq. 47 and, therefore, a tendency of a linear relationship is obtained as $n$ tends to 1.

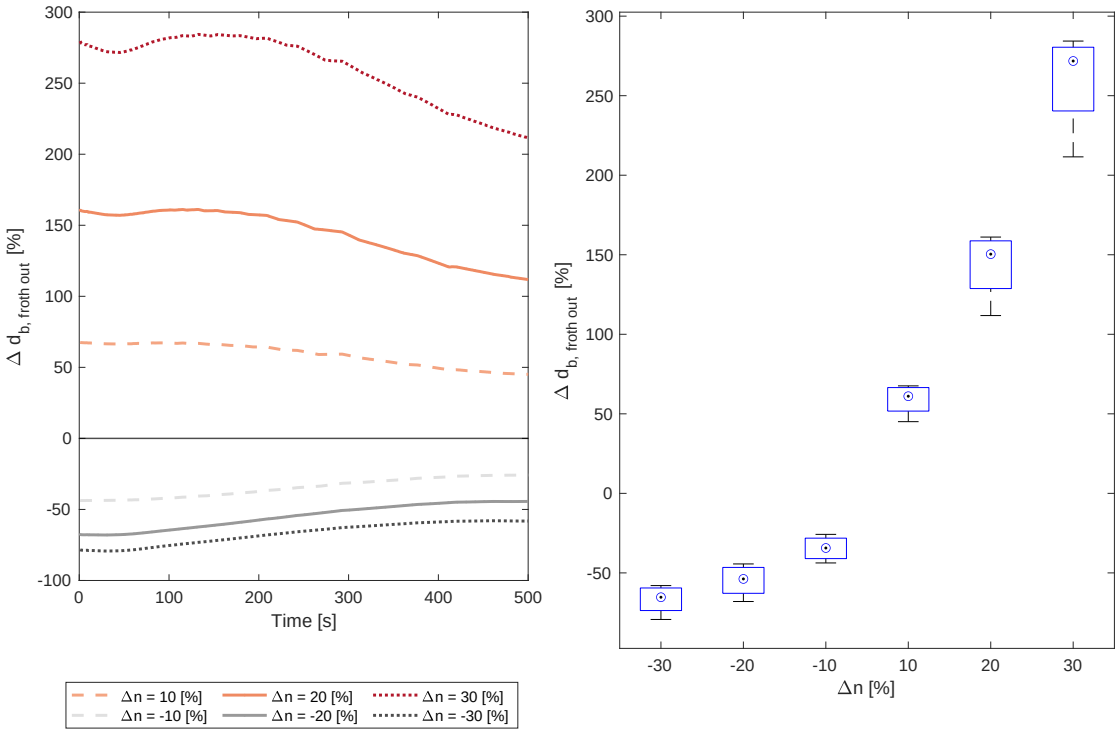


Figure 1: Sensitivity analysis of the parameter $n$ in Eq. 47, in terms of overflowing froth velocity $d_{b,\text{froth out}}$. The figure in the left shows the dynamic changes on overflowing bubble size, while the figure in the right shows the dispersion of these changes for every variation in $n$.

However, a bigger impact of $n$ is reported for the concentrate flowrate. As shown in Figure 2, the value of $n$ has an effect on the concentrate flowrate prediction up to 1600%. It seems possible that these results are due to the concentrate flowrate proportional to $\lambda_{out}$ (Eq. 46), which is inversely related to the square of $d_{b,\text{froth out}}$. Thus, $Q_{conc}$ changes drastically as $d_{b,\text{froth out}}$ varies. Note that the changes in $Q_{conc}$ decreases as $n$ approaches 2, which is the opposite effect to what happened with the overflowing froth bubble size presented previously in Figure 1. This tendency is in agreement with what was expected as $Q_{conc}$ is inverse to the square of $d_{b,\text{froth out}}$. These results revealed the high non-linearity of the fitting parameter in Eq. 47.

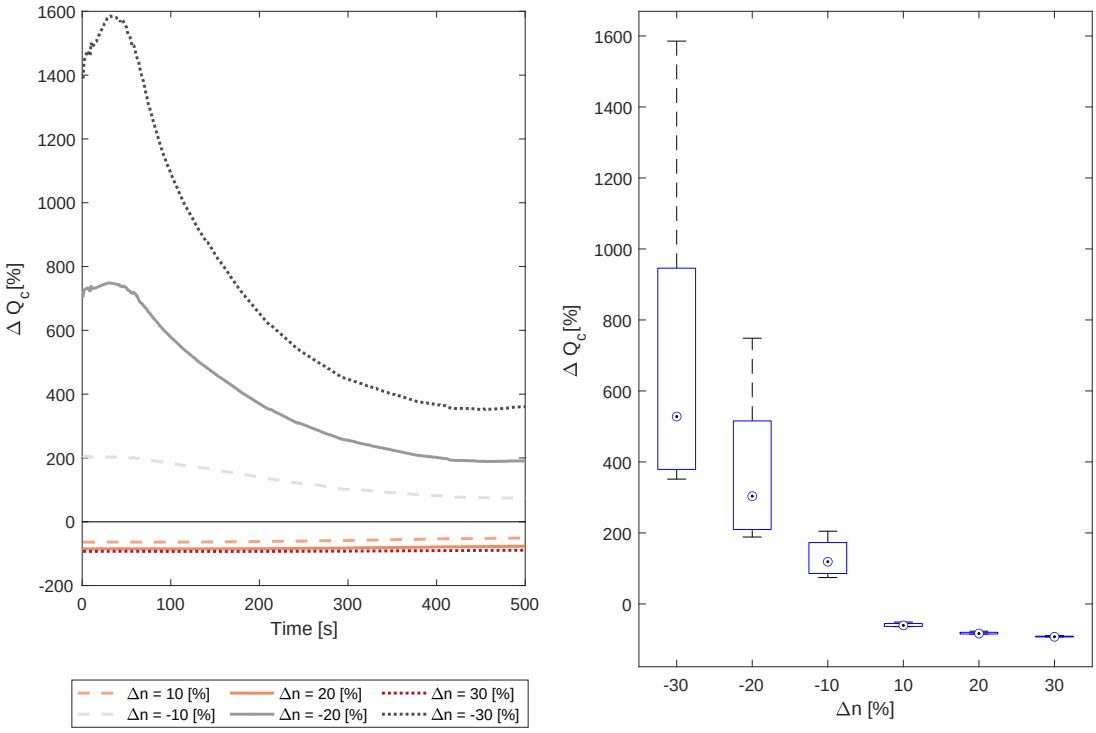


Figure 2: Sensitivity analysis of the parameter $n$ in Eq. 47, in terms of concentrate flowrate $Q_c$.

Regarding the fitting parameter $C$, the sensitivity analysis in terms of variation in the overflowing bubble size is shown in Figure 3. As can be seen from the figure, a different tendency in terms of variation of $d_{b,\text{froth out}}$ was obtained in comparison with the changes in $n$, as shown previously in Figure 1. In fact, the overflowing bubble size only varies between $\pm 35\%$, having a fairly symmetrical, flat effect for both positives and negatives changes in $C$.

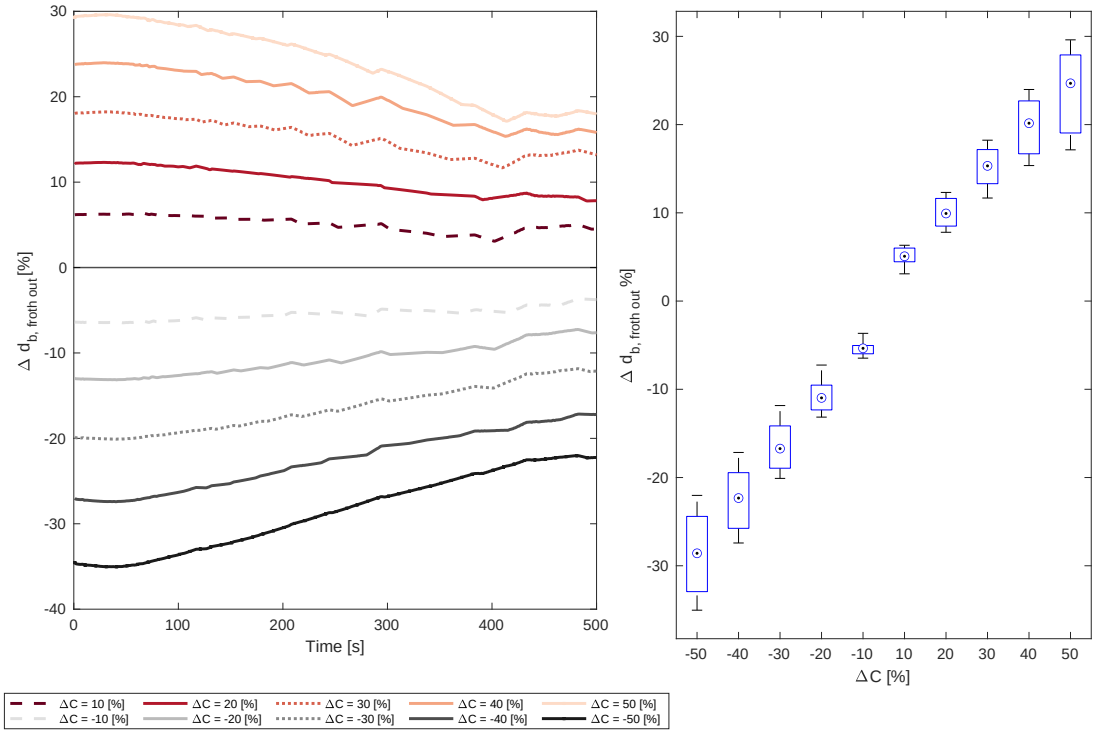


Figure 3: Sensitivity analysis of the parameter $C$ in Eq. 47, in terms of overflowing froth velocity $d_{b,\text{froth out}}$.

Figure 4 shows the sensitivity analysis for the fitting parameter $C$ with respect to changes in $Q_{conc}$. As it can be seen, a slightly greater effect is achieved for negative changes in the parameter, reaching up to 140% of changes. The box plot on the right shows that the dispersion is bigger for negative changes, especially for the dynamic part of it.

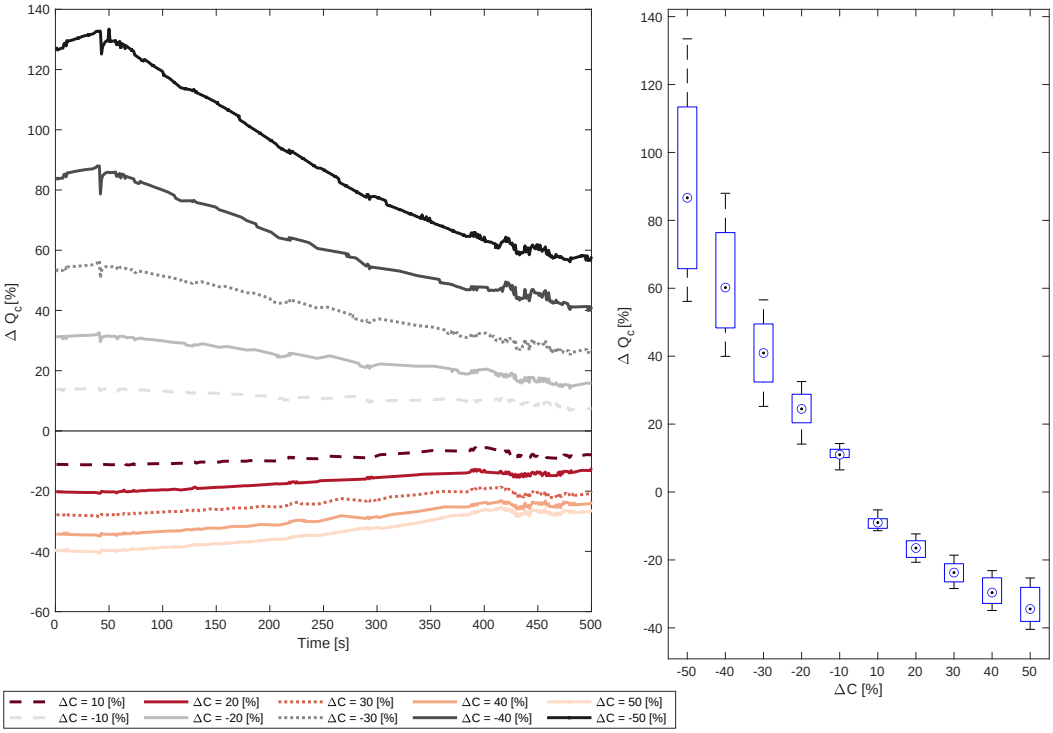


Figure 4: Sensitivity analysis of the parameter $C$ in Eq. 47, in terms of concentrate flowrate $Q_c$.

What is interesting about the sensitivity analysis for these two fitting parameters is that the changes are one order of magnitude of difference, for both variables $d_{b,\text{froth out}}$ and $Q_{conc}$. This could mean that the model calibration for Eq. 47 will be nominated by the determination of the value of $n$, which, additionally, is also restricted to have a value between 1 and 2.

Together these results of sensitivity analysis provide important insights into the model calibration methodology. It is well known that the overflowing bubble size is fairly impossible to measure directly. Therefore, an alternative approach must be applied when calibrating this model for the parameters $n$ and $C$. For example, in Part II of this paper, model calibration for $n$ and $C$ was carried out by minimising the normalised difference between the experimental and predicted (Eq. 44) concentrate flowrates. A full detailed explanation of this calibration methodology is explained in Part II of this paper.

*3.1.2. Fitting parameters a, b and c (Eq. 43):*

The bursting rate ($v_b$) can be estimated by means of the superficial gas velocity ($j_g$) as shown in Eq. 43. It has been found that a quadratic relationship between $v_b$ and $j_g$ occurs when a Peak in Air Recovery (PAR)

is found (Neethling and Brito-Parada, 2018). On the contrary, a linear relationship is likely to appear when a PAR is not clearly found.

The sensitivity analysis for the fitting parameters of the bursting rate equation, $a$, $b$ and $c$, was conducted at steady-state as the bursting rate only depends on $j_g$, which has a rapid dynamic and, thus, the steady-state value is the one that is considered. Figures 5 shows the sensitivity analysis for the three parameters for five different values of $j_g$, between 0.6 and 1.1 $[cms^{-1}]$.

The nominal values of the fitting parameters are the same as those reported in Neethling and Brito-Parada (2018). The nominal values must take into consideration the equation for air recovery (Eq. 42), because the bursting rate $v_b$ should not be greater than the superficial gas velocity $v_g^*$ (the interfacial gas velocity) to avoid air recovery to be negative. Since the interfacial gas velocity $v_g^*$ is directly related to the superficial gas velocity $j_g$ (see Eq. 22 and 37), increasing the slope means that the bursting rate also increases, reaching a value of $v_b$ greater than $v_g^*$. This implies that NaN or imaginary output values were obtained in the simulations.

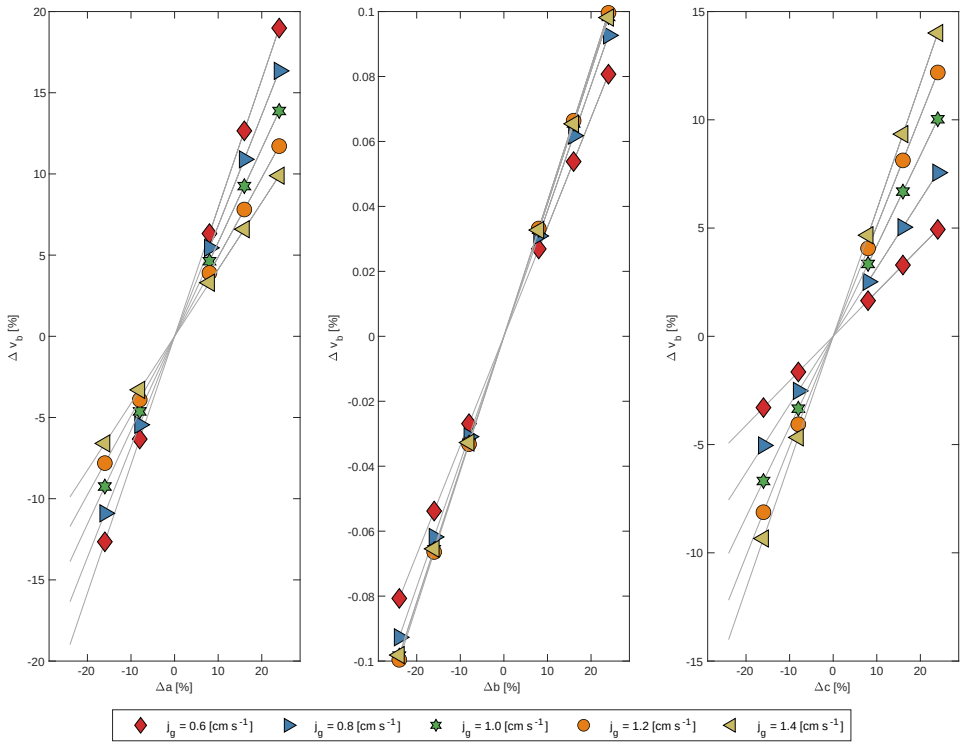


Figure 5: Sensitivity analysis of parameters $a$, $b$ and $c$ from Eq. 43, for different values of superficial gas velocity ($j_g$). The parameter $a$ corresponds to the constant term of the equation, $b$ is the lineal term, and $c$ is the quadratic term.

Similar patterns in terms of variation in $v_b$ were observed between $a$, $b$, $c$ were varied between $\pm 24\%$. However, unlike the variations in $v_b$ obtained for the parameters $a$ and $c$, a much smaller sensitivity was found for the linear parameter $b$ as the variations in $v_b$ were within $\pm 1\%$. The sensitivity analysis for the parameter $a$ in Figure 5 shows that there is a change within $\pm 20\%$ for the bursting rate, while $c$ presents a slightly lower sensibility, reporting changes between $\pm 15\%$.

Another interesting point here is to analyse the effect of the parameters $a$, $b$ and $c$ in air recovery ($\alpha^*$) from Eq. 42. Figure 6 shows the sensitivity analysis for the same range of $j_g$ as in Figure 5. Interestingly, the constant term $a$ has even a higher impact on $\alpha^*$ than $v_b$, revealing changes up to $\pm$ 50% in $\alpha^*$. While the lineal term $b$ presents a slightly higher impact on $\alpha^*$ ($\pm$ 1.5%) than $v_b$ ($\pm$ 0.1%), the quadratic term $c$ appears to have a similar impact in both $\alpha^*$ and $v_b$ (about $\pm$ 20%).

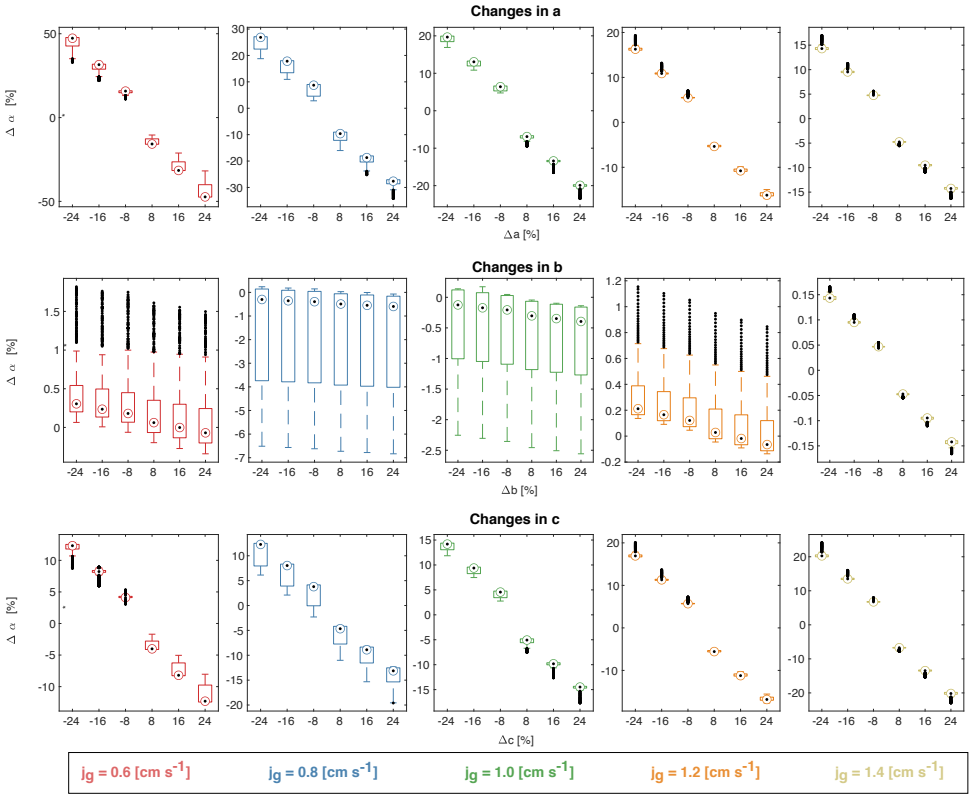


Figure 6: Sensitivity analysis of parameters $a$, $b$ and $c$ (from Eq. 43) in air recovery calculated from Eq. 42. The parameter $a$ corresponds to the constant term of the equation, $b$ is the lineal term, and $c$ is the quadratic term.

*3.1.3. Fitting parameter f (Eq. 54):*

The fitting parameter $f$ in Eq. 54 corresponds to the fraction of material that becomes detached from the bubble surfaces during coalescence. In that sense, this parameter is restricted to be between 0 and 1. A nominal value was chosen in the centre of the range, i.e. 0.5. A dynamic sensitivity analysis was performed for this parameter, varying it in ±50%.

Figure 7 shows the sensitivity analysis of the fitting parameter $f$ in terms of changes in froth recovery, $R_f$, as they are related exponentially as presented in Eq. 54. In the dynamic part of the froth recovery, $f$ has a big effect on $R_f$, up to 100 seconds. It can be also seen in the right of this figure that the changes are lower (flatter curves) when $f$ approaches 1, i.e. for positive changes.

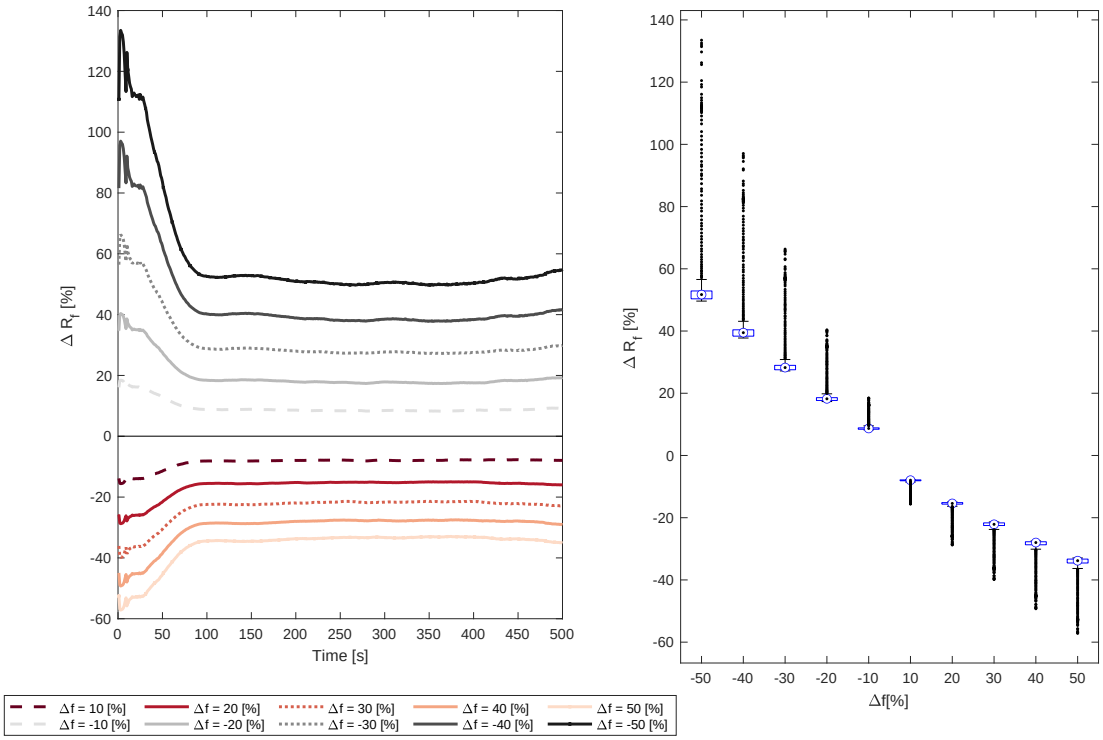


Figure 7: Sensitivity analysis of the parameter $f$ in Eq. 54, in terms of froth recovery $R_f$.

In the box plot in the right, it can be seen that the dispersion is quite small as the biggest effect in the dynamic state are taken as "outliers" (data points represented as black dots). This means that the dynamic changes are above the upper quartile for negative changes $f$, and below the lower quartile of variation for the positive changes of $f$. Taking this into consideration, the box plot results also imply that the incidence

of $f$ on $R_f$ at steady state varies to a much lesser degree, between $-30$ and 60%.

*3.1.4. Fitting parameter K:*

The fitting parameter $K$ corresponds to the number of bubble size classes in the pulp. This parameter is included in the equations for calculating gas holdup (Eq. 17), gas volume in the pulp (Eq. 14), and rise gas velocity (Eq. 32). This terms also are used to calculate important variables for predictive control, such as the pulp height (Eq. 21, 22).Therefore, a trade-off between model accuracy and elapsed time of solving the model (DAE problem) must be taken into consideration.

Since the flotation model presented in Section 2 is ultimately intended to be implemented in predictive control, the elapsed time of resolution is crucial for its implementation in real systems. In line with this, Figure 8 shows the effect of the number of bubble size classes on the elapsed resolution time. Here, it is possible to see that there is a nonlinear relation between them, having a variation of resolution time within $\pm 30\%$ with respect to the nominal value of $K$.

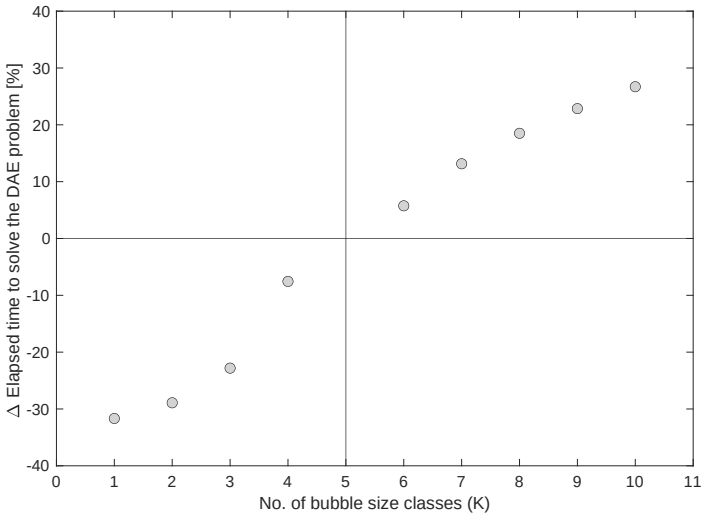


Figure 8: Changes in elapsed resolution time for the DAE problem presented in Section 2, against different number of bubble size classes ($K$). The changes were calculated with respect to a nominal value of $K = 5$.

In Part II of this paper, a model validation is made for this parameter in terms of accuracy in predicting the pulp height against experimental data.

To sum up, one of the biggest advantages of the model proposed is that it is a phenomenological model, and thus, it has as few as seven parameters to be calibrated. It also considers as input variables only those that can be easily measured at the industrial level with the instrumentation available in most of them.

### *3.2. Simulations of important variables for control*

In order to assess the model proposed, simulations for different $j_g$ and $Q_{feed}$ were performed. These two variables were chosen as the air flowrate $Q_{air,in}$, and thus $j_g$, is usually a manipulated variable; while $Q_{feed}$ for the first cell of a flotation bank can be considered as a disturbance of the process as it depends on what is happening upstream, and it cannot be controlled. The simulations performed in this section allow understanding the behaviour and adaptability of the model to changes in operating conditions.

#### *3.2.1. Gas holdup:*

Figure 9 shows the dynamics of the total gas holdup ($\varepsilon_0^{total}$, from Eqs. 17 and 18) for different values of $j_g$. In this case, it can be seen that the dynamics are rather flat in all cases. Greater changes in dynamics are reported as $j_g$ increases. This is because the gas holdup is a state in the model and, therefore, it strongly depends on the initial conditions. As the initial conditions for all cases was the same, i.e. gas holdup calculated at $j_g = 0.6$ $[cms^{-1}]$, the starting point is significantly lower when compared to that obtained at higher $j_g$.

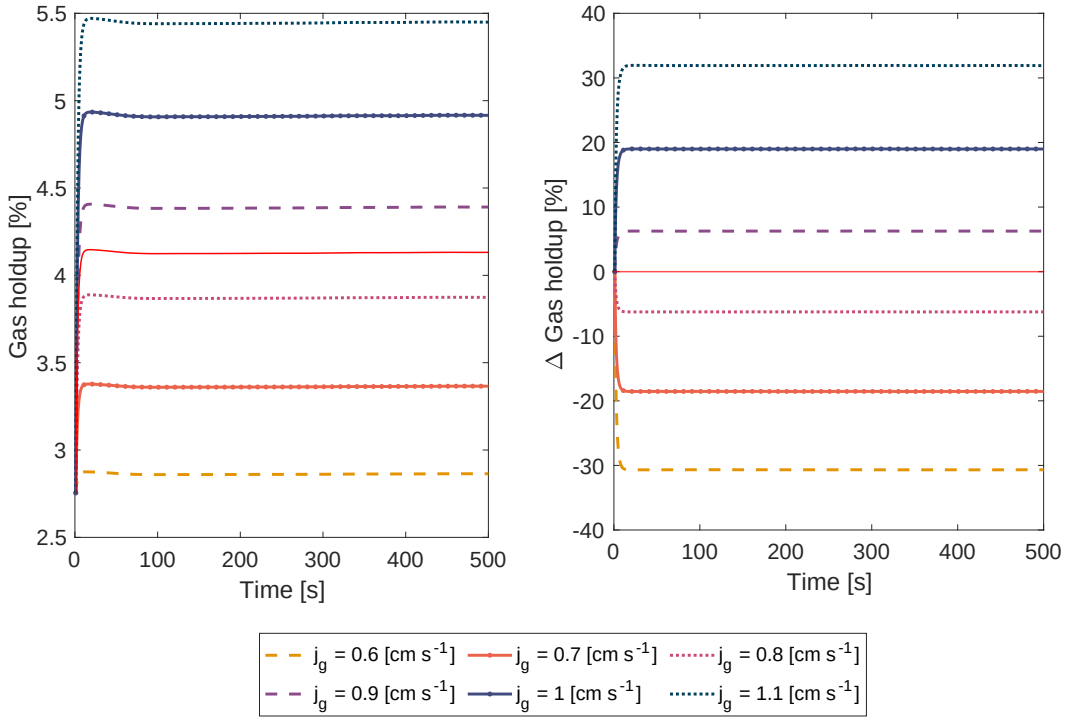


Figure 9: Left: Total gas holdup dynamics for different values of $j_g$. Right: Dynamic changes in the gas holdup with respect to the nominal value. The red solid lines indicate the total gas holdup dynamics for the nominal value of $j_g$, which is equal to 0.85 $[cms^{-1}]$. The total gas holdup was simulated using Eq. 17, maintaining constant all inputs variables, except for $Q_{air,in}$.

Although the gas holdup model (Eq. 17) also depends on the in and out flowrates, i.e. $Q_{feed}$, $Q_{tailings}$ and $Q_{conc}$, this term did not affect significantly the calculation of gas holdup. As can be seen in Figure 10, there is no difference when applying disturbances for $Q_{feed}$, maintaining all other inputs variables constant. The differences in gas holdup calculated were in a range of $\pm 0.15\%$.

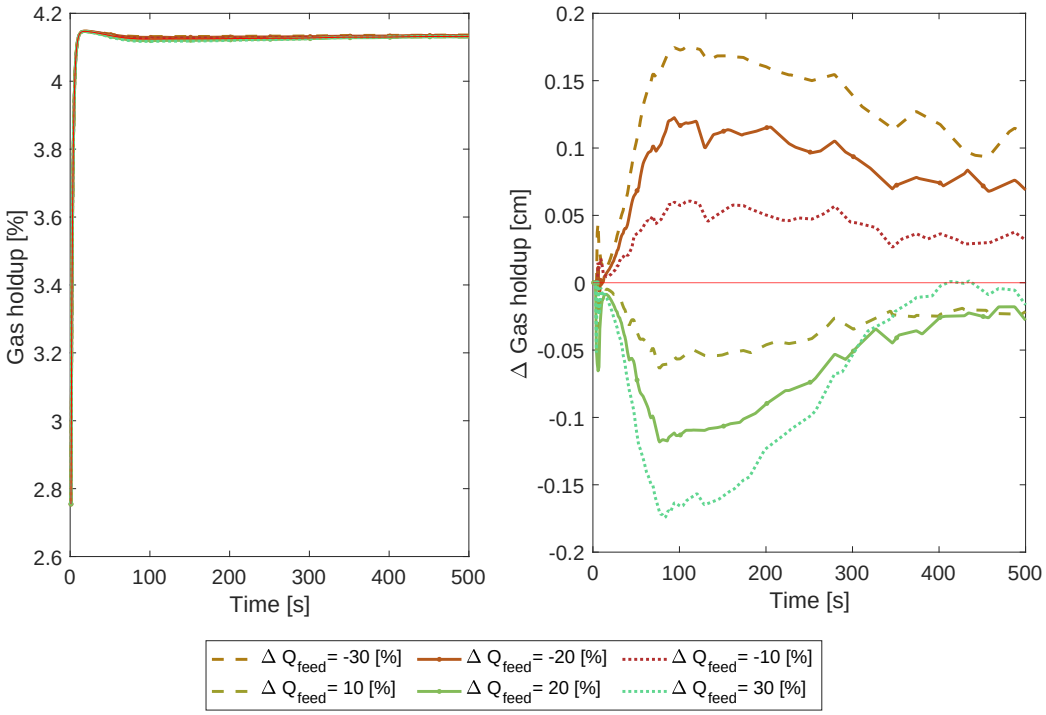


Figure 10: Left: Total gas holdup dynamics for different values of $Q_{feed}$, calculated using Eq. 17, without manipulating $Q_{tailings}$. Right: Dynamic changes in the gas holdup with respect to the nominal value. The red solid lines indicate the total gas holdup dynamics for the nominal value.In all cases, $j_g$ was maintained constant at 0.85 $[cms^{-1}]$.

### *3.2.2. Air recovery:*

Figure 11 shows the changes in air recovery (left) and metallurgical recovery (right) with respect to changes in $j_g$. The metallurgical recovery was calculated as the mass of valuable mineral reported in the concentrate via true flotation (Eq. 51) and entrainment (Eq. 56), divided by the valuable mineral entering into the flotation cell (Eq. 10).

A clear Peak Air Recovery (PAR) was found at $j_g = 0.9$ $[cms^{-1}]$, which is the same air rate at which a maximum metallurgical recovery is located. This result further supports the idea that a PAR is translated to an increase in the metallurgical recovery, as reported in Hadler and Cilliers (2009); Hadler et al. (2010); Shean et al. (2017); Neethling and Brito-Parada (2018). A PAR can be found when the bursting rate ($v_b$ from Eq. 43) presents a quadratic dependency on $j_g$, as demonstrated by Neethling and Brito-Parada (2018). In this current study, we have used the same parameters $a$, $b$ and $c$ as those presented by Neethling and Brito-Parada (2018), which are also the same used for the sensitivity analysis of the parameters in Section

3.1.

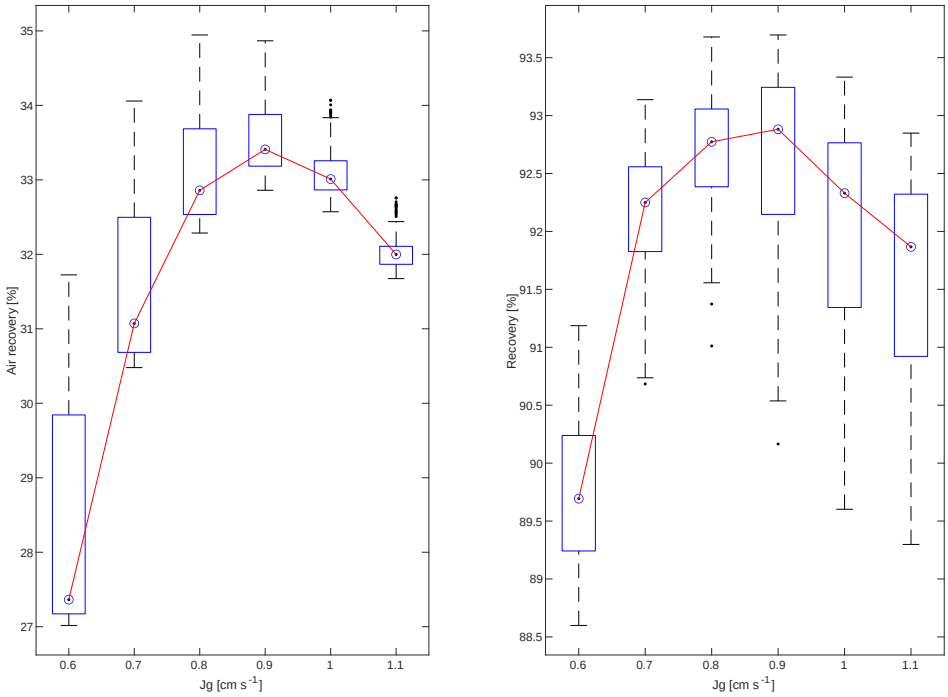


Figure 11: Air recovery (from Eq. 42) and metallurgical recovery as a function of $j_g$. The central points in the box plot are the median of the air recovery. The red lines represent the tendency of the median values for both air recovery and metallurgical recovery.

Interestingly, a PAR was also found even when the $j_g$ was kept constant at 0.85 $[cms^{-1}]$, as shown in Figure 13. However, the tendency is not as clear as to when changes in $j_g$ were performed, as presented in Figure 11. It can be also seen that although a PAR is found for $\Delta Q_{feed} = 30\%$ in the dynamic part, it drops drastically at steady-state. This is a significant outcome that must be taken into consideration when implementing the model into control strategies. This result suggests that $Q_{feed}$ should be measured online and used – or at least, accurately estimated – to properly update the model in the control strategy.

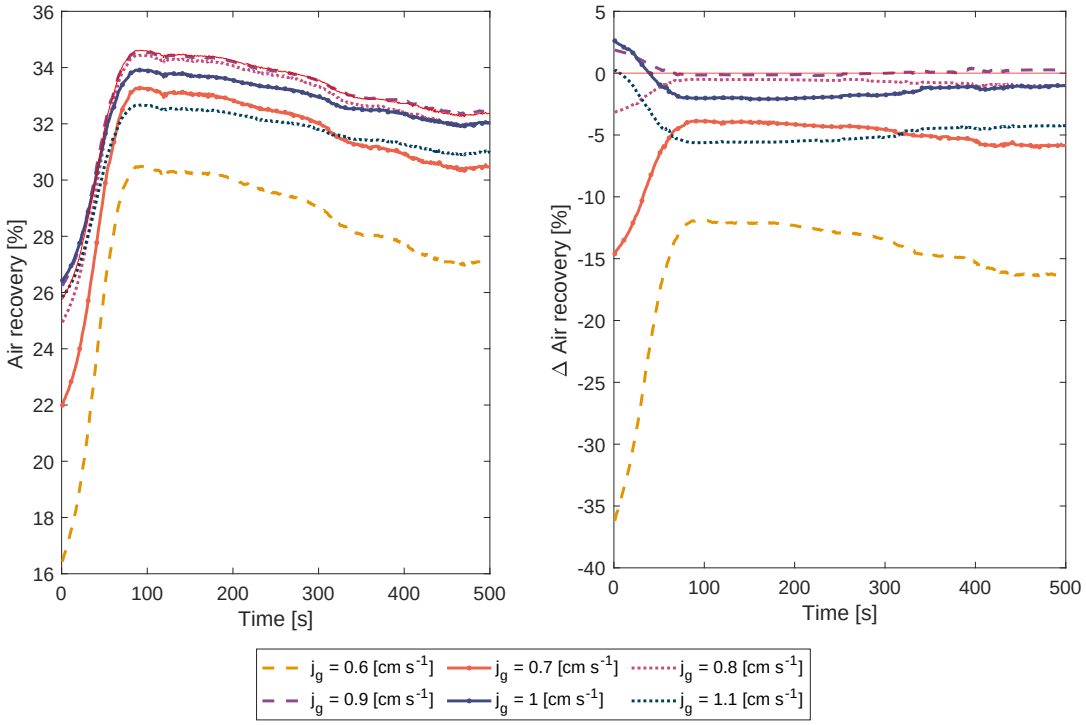


Figure 12: Left: Air recovery dynamics for different values of $j_g$. Right: Dynamic changes in air recovery with respect to the nominal value, which is $j_g = 0.85$ $[cms^{-1}]$.The red solid lines indicate the total gas holdup dynamics for the nominal value.

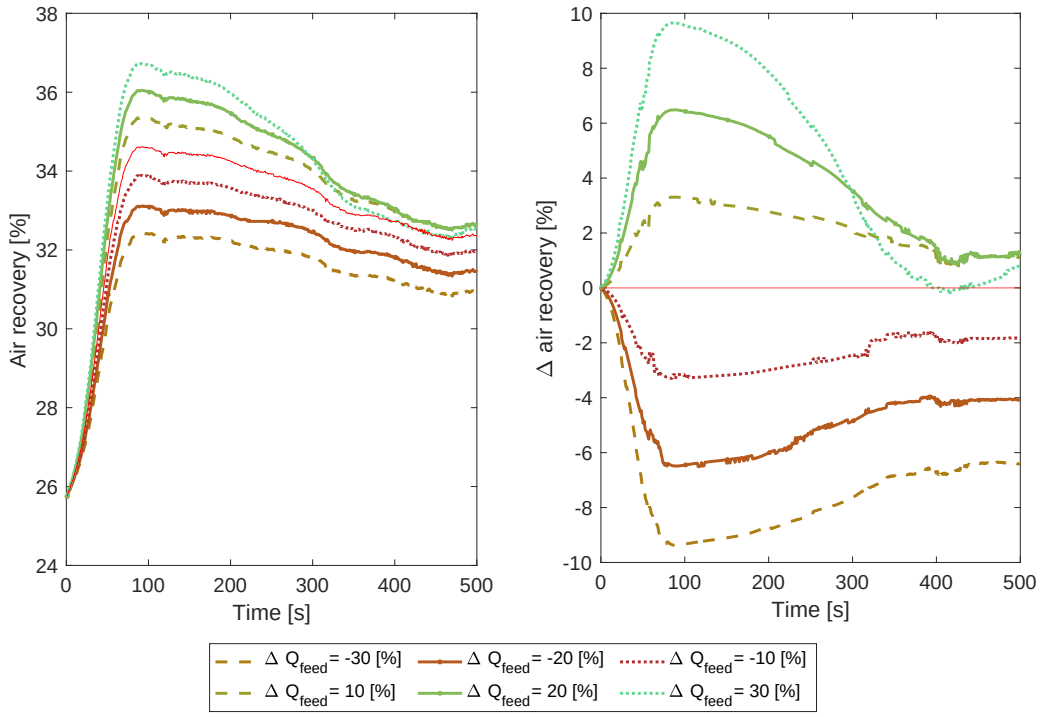


Figure 13: Left: Air recovery dynamics for different values of $Q_{feed}$. Right: Dynamic changes in air recoverywith respect to the nominal value. In all cases, $j_g$ was maintained constant at 0.85 $[cms^{-1}]$. The red solid lines indicate the total gas holdup dynamics for the nominal value.

In order to assess the adaptability and capability of prediction of the model proposed, random perturbations in $j_g$ were also applied into the simulations. As an example, Figure 14 presents the dynamic changes of gas holdup and air recovery when $j_g$ varies. As can be seen from the figure, the model responds rapidly to changes in both variables. The dotted line in the air recovery (centre) represents the air recovery calculated using Eq. 39, while the solid line is the air recovery using Eq. 42. The most notorious finding to emerge from this analysis is that both models for air recovery are able to predict it in the same direction.

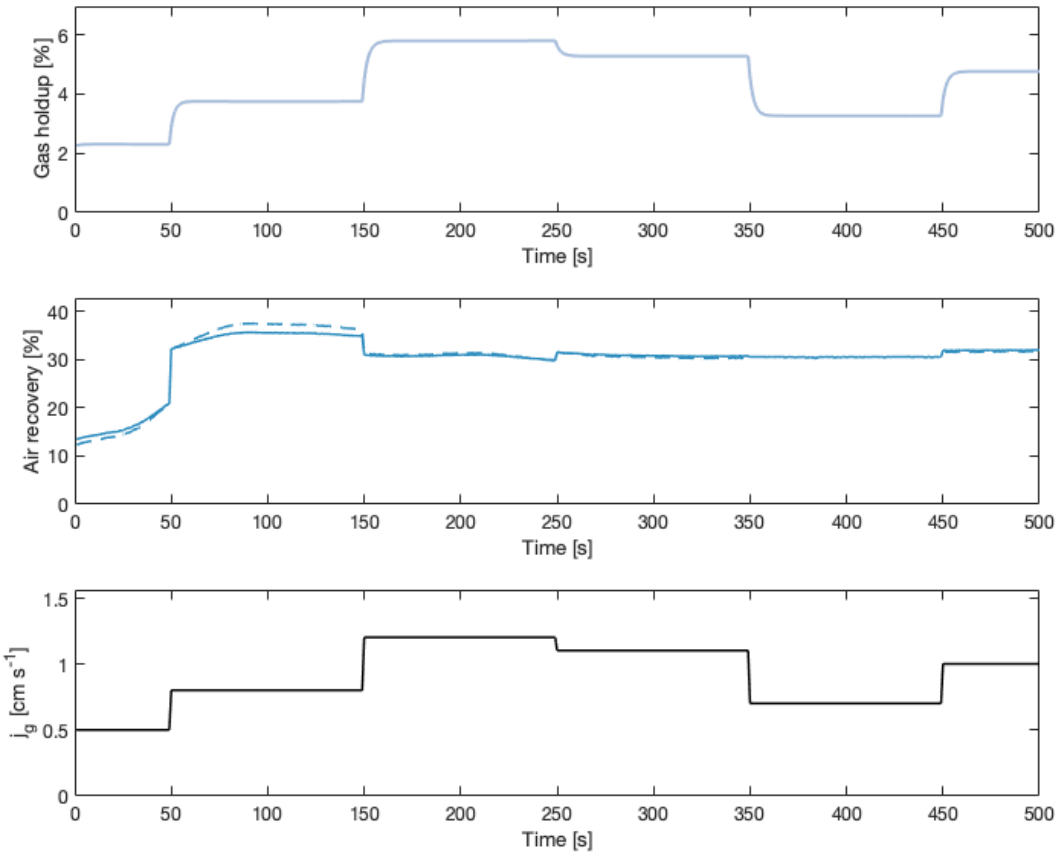


Figure 14: Dynamic changes in gas holdup (top) and air recovery (centre) with respect to changes in $j_g$ (bottom). All other input variables were maintained constant during the simulation. The dotted line in the air recovery (centre) represents the air recovery calculated using Eq. 39, while the solid line is the air recovery using Eq. 42.

### *3.2.3. Concentrate flowrate:*

Water recovery in a flotation cell is an important variable as it is related to the amount of gangue reported to the concentrate by entrainment. This variable can be estimated by means of Eq. 44 (Neethling and Cilliers, 2009). In the current study, it was assumed that $Q_l$ is approximately equalled to $Q_{conc}$. This assumption has been also made by previous studies, such as those found in Hu et al. (2013); Oosthuizen et al. (2021). For this reason, Figure 15 presents the concentrate flowrate dynamics with respect to changes in $j_g$, while Figure 16 stands for changes in $Q_{feed}$. The images on the left of both figures are the difference in $Q_{conc}$ with respect to the nominal value. In both cases, $Q_{conc}$ has a significant difference from their nominal value of up to 250%.

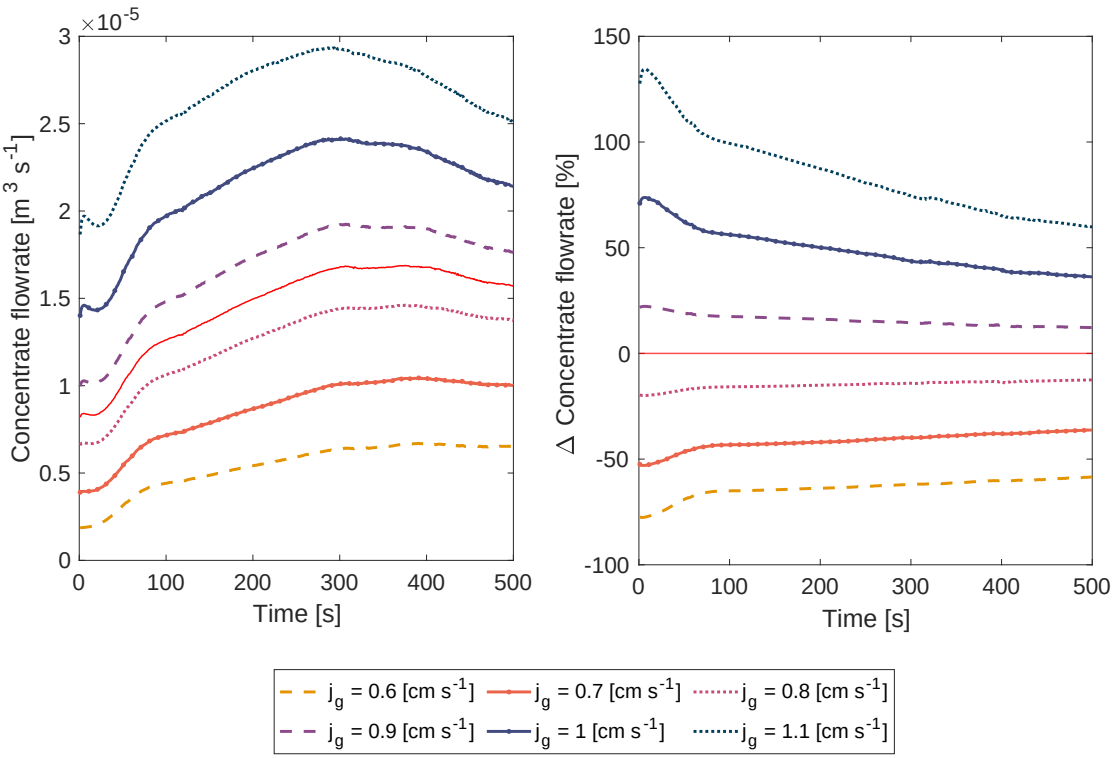


Figure 15: Left: Concentrate flowrate dynamics for $j_g$ values between 0.6 and 1.1 $[cms^{-1}]$. Right: Dynamic changes in concentrate flowrate with respect to the nominal value. The red lines indicate the total gas holdup dynamics for the nominal value of $j_g$, which is equal to 0.85 $[cms^{-1}]$. The total gas holdup was simulated using Eq. 17, maintaining constant all inputs variables, except for $Q_{air,in}$.

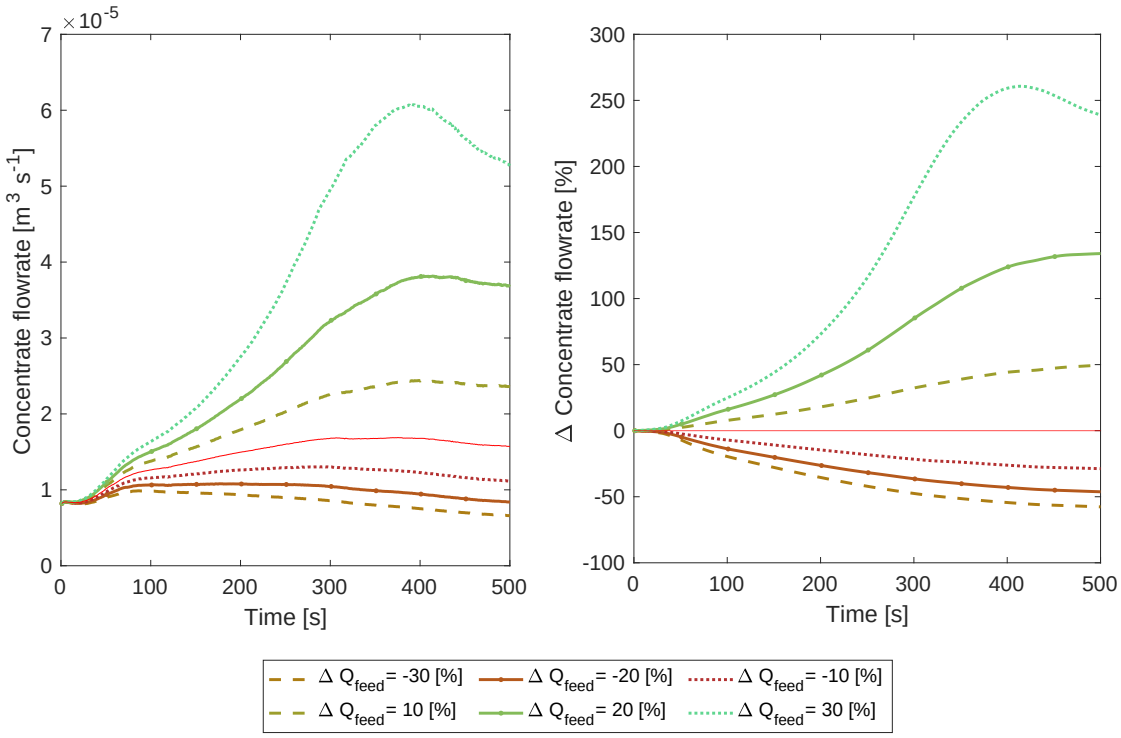


Figure 16: Left: Concentrate flowrate dynamics for different values of $Q_{feed}$, calculated using Eq. 44, without manipulating $Q_{tailings}$. Right: Dynamic changes in concentrate flowrate with respect to the nominal value. The solid red lines in both images represent the $Q_{conc}$ calculated the nominal value of $Q_{feed}$. In all cases, $j_g$ was maintained constant at 0.85 $[cms^{-1}]$.

### *3.2.4. Pulp height:*

As mentioned in Section 2, a "gas free" pulp height ($h_0$) was defined by means of Eq. 19, while the actual pulp height ($h_p$), from Eq. 21, was defined by considering also the volume of gas in the pulp (Shean et al., 2018). Figure 17 shows the dynamics of both $h_0$ and $h_p$, in which it can be concluded that both variables have the same tendency, meaning that the gas holdup dynamics does not have a huge impact on the tendency of $h_p$. However, the actual final value for pulp height increments, as expected, due to the volume occupied by the gas. These increments significantly affect the froth depth as for example, in the nominal value (solid red lines in the figures), the froth depth can go from 4 to 2 [cm] plus the froth height above the cell lip (the total height for the flotation cell simulated was 48 [cm]). This is a change in 50% in froth depth, which is translated as a big effect on the froth itself.

The pulp height goes through a maximum in all cases, in time between 300 to 400 seconds. This means that the concentrate flowrate has a major impact in the overall mass balance in those times. This, in fact,

is in line with what can be seen in Figure 12, where the concentrate flowrate start to be higher as well. This tendency is explained by the fact that the simulations were carried out considering an experimental rig, which obviously has different dimensions from those found in industry.

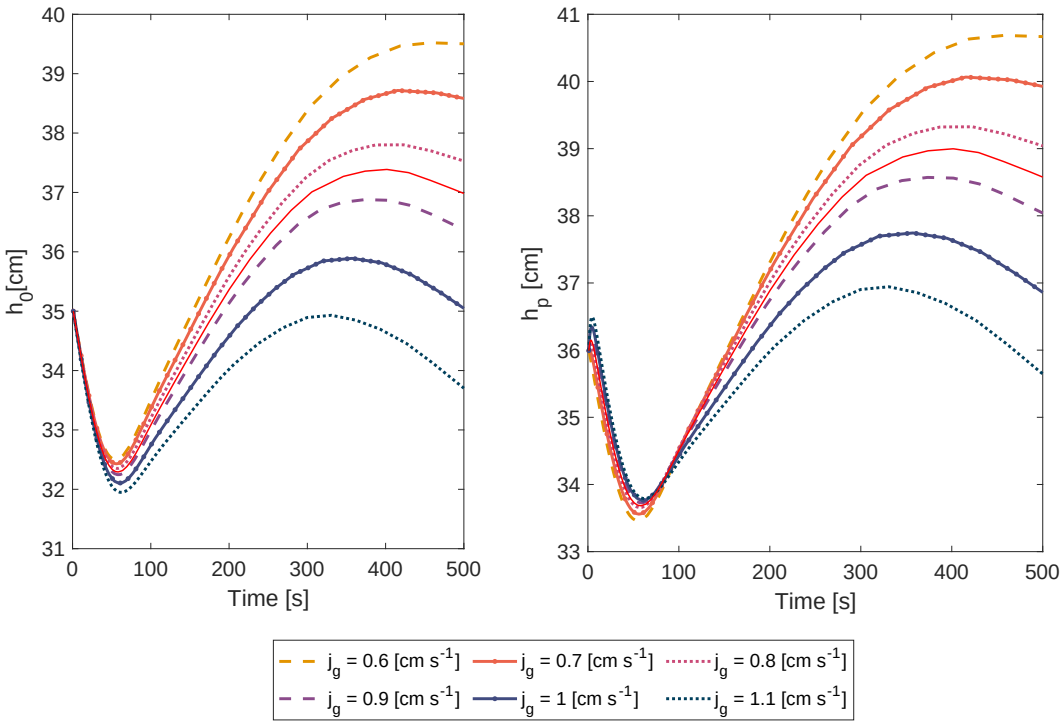


Figure 17: Dynamics of the gas free pulp height ($h_0$, from Eq. 19) and the actual pulp height ($h_p$, from Eq. 21 and 22), for $j_g$ values between 0.6 and 1.1 $[cms^{-1}]$. The solid red lines indicate the dynamics of $h_0$ and $h_p$, respectively, calculated at nominal value of $j_g$, which is equal to 0.85$[cms^{-1}]$. All these variables were simulated by maintaining constant all inputs variables, except for $Q_{air,in}$.

Disturbances in $Q_{feed}$ will also have an obvious impact on pulp height if the tailings flowrate is not manipulated. Figure 18 shows the dynamics of the actual value of pulp height ($h_p$) when varying $Q_{feed}$ without manipulating $Q_{tailings}$. As expected, there is a relatively great effect on the pulp height due to volume balance over the flotation cell.

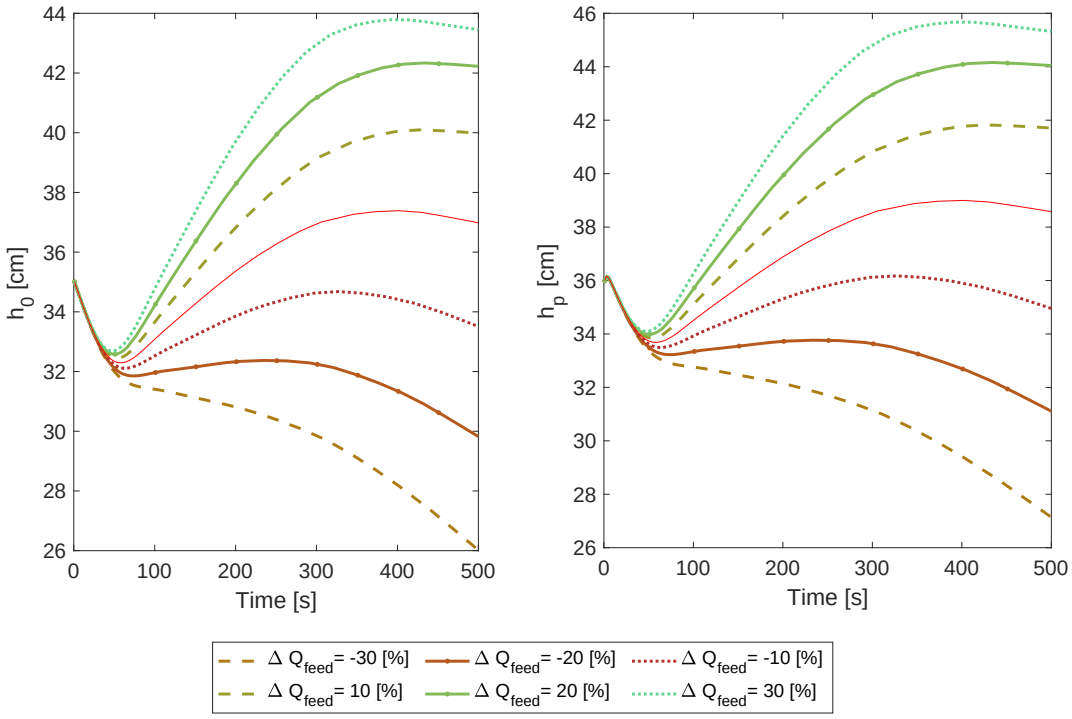


Figure 18: Left: Pulp height dynamics for different values of $Q_{feed}$ without manipulating $Q_{tailings}$. Right: Dynamic changes in the pulp height with respect to the nominal value. The solid red lines in both images represent the $h_0$ and $h_p$, respectively, calculated at the nominal value of $Q_{feed}$.

### *3.2.5. Overflowing froth bubble size:*

Overflowing bubble size ($d_{b,\text{froth out}}$, from Eq. 47) plays an important role in water recovery, as the $Q_{conc}$ in Eq. 44 is inverse of the square of $d_{b,\text{froth out}}$. Nevertheless, the overflowing bubble size presented in this current study should not be confused with the bubble size on the top of the froth, like the one used in the model presented by (Oosthuizen et al., 2021). It has been demonstrated that the bubble sizes at the lip and the top can vary significantly due to bubble coalescence, especially when the froth height above the lip is big. However, the overflowing bubble size (at the cell lip) is fairly impossible to measure, and some considerations must be taken when calibrating this model. A further explanation regarding the model calibration is presented in Part II of this paper.

As can be seen from Figure 19, the overflowing bubble size has rapid dynamics, having a peak before the steady state. The bubble sizes are usually smaller than 1 [cm] (Neethling and Cilliers, 2008). This variable depends on the mean froth residence time and the interface bubble sizes. As the mean froth residence time

depends on $j_g$, the overflowing bubble size also depends on this variable. The image in the right in Figure 19 shows that those variation can go between $-15$ to 25%, for a range of $j_g$ between 0.6 and 1.1 $[cms^{-1}]$.

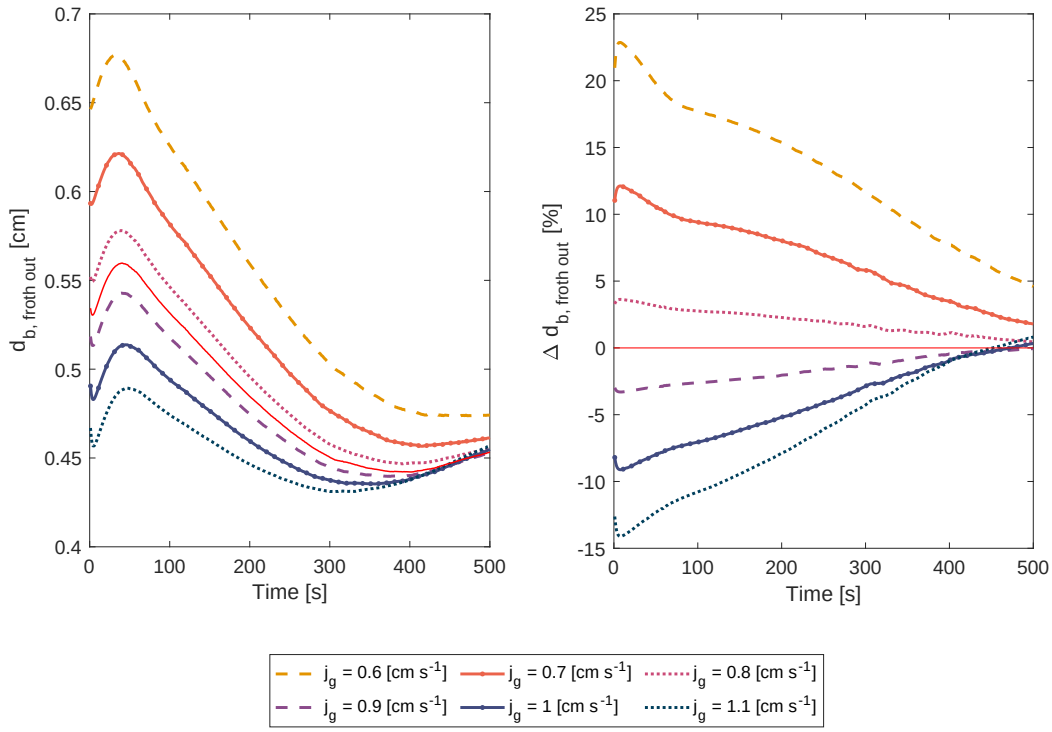


Figure 19: Left: Overflowing froth bubble size dynamics for $j_g$ values between 0.6 and 1.1 $[cms^{-1}]$. Right: Dynamic changes in the overflowing froth bubble size with respect to their nominal value, calculated at $j_g = 0.85[cms^{-1}]$. The solid red lines in both images represent the overflowing froth bubble size calculated at the nominal value of $j_g$. The overflowing froth bubble size was simulated using Eq. 47, maintaining constant all inputs variables, except for $Q_{air,in}$.

Surprisingly, much larger differences from their nominal value were found when $Q_{feed}$ was varied, as shown in Figure 20. This is because the model $d_{b,\text{froth out}}$ depends on the mean froth residence time, which depends on the froth depth ($h_f$). A simple volume balance over the flotation cell clearly states that the froth depth is defined by the flowrates entering and leaving the cell, therefore, $Q_{feed}$ has an evident impact on it. This result suggests, once more, that $Q_{feed}$ should be measured online and used – or at least, accurately estimated – to properly update the model in the control strategy.

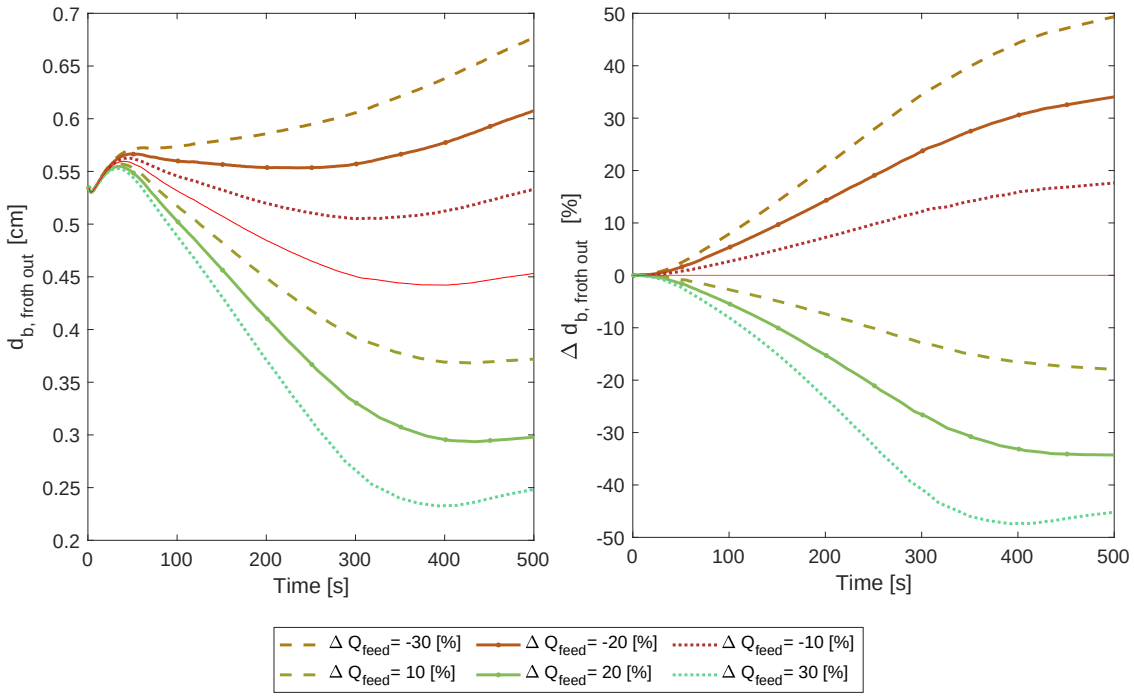


Figure 20: Left: Overflowing froth bubble size dynamics for different values of $Q_{feed}$ without manipulating $Q_{tailings}$. $d_{b,\text{froth out}}$ was calculated using Eq. 47. Right: Dynamic changes in the overflowing froth bubble size dynamics with respect to the nominal value. The red lines in both images represent the overflowing froth bubble size calculated at the nominal value of $Q_{feed}$. In all cases, $j_g$ was maintained constant at 0.85 $[cms^{-1}]$.

## 4. Conclusions

Although froth stability has vital importance on the overall performance of the flotation process, few studies have attempted to incorporate it in models for predictive control strategies. Froth stability can be incorporated by considering the froth physics as it is utilised to estimate the valuable material that reports to the concentrate. This estimation, in turn, can be used in control strategies as a proxy to calculate performance indicators, such as grade and recovery.

In this study we present a complete dynamic flotation model to be implemented in model predictive control strategies. Unlike other models for control in the literature, the model presented here is, to the best of the authors' knowledge, the first of its kind to incorporate measurements of froth stability via air recovery, bursting rate, and bubble coalescence model equations, along with those presented for the pulp-froth interface.

This first part of the paper presents a detailed description of the model development. A sensitivity analysis of the parameters of the model and simulations of important control variables were performed in order to assess the predictive capability of the model. This study has identified that seven parameters must be calibrated to use the model effectively. From the sensitivity analysis it can be concluded that the parameter $n$ of the equation for the overflowing bubble size (Eq. 47), and $a$ and $c$ of the equation for the bursting rate (Eq. 43) are the most sensitive parameters. Although the sensitivity of the other four parameters was lower, the results showed that there will still be a significant difference in the prediction accuracy if the parameters were poorly estimated.

One of the biggest advantages of the model proposed here is that it is a phenomenological model. This means that it can be successfully implemented to a wide range of operating conditions. In order to verify its robustness, simulations were performed by considering variations in air flowrate, and disturbances in feed flowrate. This analysis revealed that that the model is capable of reacting correctly under disturbances and changes in operating conditions.

Additionally, it was shown, via an analysis of degrees of freedom, that two variables from the model can be used as manipulated variables for control. The most commonly manipulated variables in a flotation cell are the tailings flowrate and air flowrate, which means that future work will focus on the implementation of this model into MPC strategies, considering these two manipulated variables. In Part II of this paper, we present the model calibration and validation, along with the experimental procedure performed for this purpose.

## 5. Appendix

Table 5: Variables of the model, nomenclature, units, and total number of variables to be included in the analysis of degree of freedom in Section 3

| No. | Variable | Symbol | Units | Number of variables |
|---|---|---|---|---|
| 1 | Air recovery | $\alpha$ | – | 1 |
| 2 | Axial dispersion | $D_{axial}$ | – | 1 |
| 3 | Bubble size in the froth (overflowing) | $d_{b,froth}$ | $m$ | 1 |
| 4 | Bubble surface area flux | $S_b$ | $1/s$ | 1 |
| 5 | Bursting rate | $v_b$ | $m/s$ | 1 |
| 6 | Concentrate flowrate | $Q_{conc}$ | $m^3/s$ | 1 |
| 7 | Control valve output for the tailings flowrate | $u_v$ | – | 1 |
| 8 | Entrainment factor | $ENT_i$ | – | $i$ |

**Table 5 continued from previous page**

| | | | | |
|---|---|---|---|---|
| 9 | Feed flowrate | $Q_{feed}$ | $m^3/s$ | 1 |
| 10 | Flotation rate constant | $k_i$ | $1/s$ | $i$ |
| 11 | Froth depth | $h_f$ | $m$ | 1 |
| 12 | Froth recovery | $R_{f,i}$ | $-$ | $i$ |
| 13 | Froth velocity over the lip | $v_f$ | $m/s$ | 1 |
| 14 | Froth-phase air recovery | $\alpha^*$ | $-$ | 1 |
| 15 | Gas flowrate into the cell (total) | $Q_{air,in}$ | $m^3/s$ | 1 |
| 16 | Gas flowrate for each bubble size class | $Q^k_{air,in}$ | $m^3/s$ | $K$ |
| 17 | Gas free pulp height | $h_0$ | $m$ | 1 |
| 18 | Gas hold-up for each bubble size class | $\varepsilon^k_0$ | $-$ | $K$ |
| 19 | Gas velocity out of the pulp for each bubble size class | $v^k_{g,\text{out pulp}}$ | $m/s$ | $K$ |
| 20 | Gas volume of each bubble size class in the pulp phase | $V^k_{gas}$ | $m^3$ | $K$ |
| 21 | Head grade (mineral concentration) | $C_{i,f}$ | $kg/m^3$ | $i$ |
| 22 | Interfacial gas rate | $v^*_g$ | $m/s$ | 1 |
| 23 | Length of Plateau borders per volume of foam | $\lambda_{out}$ | $1/m^2$ | 1 |
| 24 | Mean bubble size in the interface | $d_{b,int}$ | $m$ | 1 |
| 25 | Particle size per mineralogical class | $d_{p,i}$ | $m$ | $i$ |
| 26 | Physical parameter | $k_1$ | $m/s$ | 1 |
| 27 | Proportion of bubble size classes in the pulp | $\Psi^k_{d_{b,pulp}}$ | $-$ | $K$ |
| 28 | Pulp flowrate out of the cell | $Q_{pulp,out}$ | $m^3/s$ | 1 |
| 29 | Pulp height | $h_p$ | $m$ | 1 |
| 30 | Pulp volume in the cell | $V_{pulp}$ | $m^3$ | 1 |
| 31 | Residence time in the froth | $\tau_f$ | $s$ | 1 |
| 32 | Settling velocity | $v_{set}$ | $m/s$ | $i$ |
| 33 | Slurry content | $\epsilon$ | $-$ | 1 |
| 34 | Slurry density | $\rho_{pulp}$ | $kg/m^3$ | 1 |
| 35 | Slurry viscosity | $\mu_{pulp}$ | $kg/ms$ | 1 |
| 36 | Solid concentration in the tailings | $C_{i,tailings}$ | $kg/s$ | $i$ |
| 37 | Solid flowrate in the concentrate due to entrainment | $m_{i,ENT}$ | $kg/s$ | $i$ |
| 38 | Solid flowrate in the concentrate due to true flotation | $m_{i,TF}$ | $kg/s$ | $i$ |
| 39 | Solid mass flowrate in the feed | $m_{i,feed}$ | $kg/s$ | $i$ |
| 40 | Solid mass flowrate in the tailings | $m_{i,tailings}$ | $kg/s$ | $i$ |
| 41 | Solid mass in the pulp phase | $M_i$ | $kg$ | $i$ |

**Table 5 continued from previous page**

| | | | | |
|---|---|---|---|---|
| 42 | Superficial gas velocity | $j_g$ | $m/s$ | 1 |
| 43 | Tailings flowrate | $Q_{tailings}$ | $m^3/s$ | 1 |
| 44 | Total gas hold-up | $\varepsilon_{0,total}$ | $-$ | 1 |
| 45 | Total gas velocity out of the pulp | $v^{total}_{g,\text{out pulp}}$ | $m/s$ | 1 |
| 46 | Total gas volume in the pulp phase | $V_{gas}$ | $m^3$ | 1 |
| | | **Total number of variables** | | $29 + 12\ i + 5\ K$ |

Table 6: Model equations for each variable, including their classification. The last column refers to the total number of equations for each variable to be included in the analysis of degrees of freedom in Section 3 .

| Variable | Equation | Type of equation | Number of equation(s) |
|---|---|---|---|
| Conservation of mass | $\frac{dM_i}{dt} = m_{i,feed} - m_{i,tailings} - m_{i,TF} - m_{i,ENT}$ | Phenomenological | $i$ |
| | *Pulp phase* | | |
| Air flowrate of each bubble size class | $Q^k_{air,in} = Q_{air,in}\Psi^k_{d_{b,pulp}}$ | Semi-empirical | $K$ |
| Flowrate out of the flotation tank | $Q_{\text{pulp,out}} = Q_{\text{tailings}} + Q_{\text{conc}}$ | Phenomenological | 1 |
| Gas holdup | $\frac{d\left(\frac{\varepsilon^k_0}{1-\varepsilon_{0,\text{total}}}\right)}{dt} = \frac{1}{h_0}\left(\frac{Q^k_{\text{air},in}}{A} - v^k_{\text{g,out pulp}}\varepsilon^k_0\right) - \frac{1}{h_0}\left(\frac{Q_{\text{feed}}}{A_{\text{cell}}} - \frac{Q_{\text{pulp,out}}}{A_{\text{cell}}}\right)\left(\frac{\varepsilon^k_0}{1-\varepsilon_{0,\text{total}}}\right)$ | Phenomenological | $K$ |
| Gas volume of each bubble size class | $V^k_{gas} = \frac{\varepsilon^k_0}{1-\varepsilon^k_0}h_0 A_{cell}$ | Phenomenological | $K$ |
| Gas-free pulp height | $\frac{dh_0}{dt} = \frac{Q_{feed}}{A_{cell}} - \frac{Q_{pulp,out}}{A_{cell}}$ | Phenomenological | 1 |
| Proportion of each bubble size class | $\Psi^k_{d_{b,pulp}} = \frac{(\text{frequency bubble size class})_k}{\sum_{k=1}^{K}(\text{frequency bubble size class})_k}$ | Empirical | $K$ |
| Pulp density | $\rho_{\text{pulp}} = \phi\rho_{\text{sol}} + (1-\phi)\rho_{\text{water}}$ | Phenomenological | 1 |
| Pulp height | $h_p = \frac{h_0}{1-\varepsilon_{0,\text{ total}}}$<br>ODE form (combining Eqs. for $h_0$ and gas holdup):<br>$\frac{dh_p}{dt} = \frac{1}{A_{cell}}(Q_{feed} - Q_{pulp,out})\left(\frac{1}{1-\sum_{k=1}^{K}\varepsilon^k_0}\right) + \frac{h_0}{\left(1-\sum_{k=1}^{K}\varepsilon^k_0\right)}\sum_{k=1}^{K}\frac{d\varepsilon^k_0}{dt}$ | Phenomenological | 1 |
| Pulp viscosity | $\mu_{\text{pulp}} = \mu_{\text{water}}\exp\left(\frac{2.5\phi}{1-0.609\phi}\right)$ | Empirical | 1 |
| Pulp volume (liquid + gas) | $V_{pulp} = h_0 A_{cell} + V_{gas}$ | Phenomenological | 1 |
| Solid mass flowrate in the feed | $m_{i,feed} = C_{i,f}Q_{feed}$ | Phenomenological | $i$ |
| Solid mass flowrate in the tailings | $m_{i,tailings} = C_{i,tailings}Q_{tailings}$ | Phenomenological | $i$ |
| Superficial gas velocity | $j_g = Q_{air}A_{cell}$ | Phenomenological | 1 |
| Tailings particle concentration | $C_{i,tailings} = \frac{M_i}{V_{pulp}}$ | Phenomenological | $i$ |
| Total gas holdup | $\varepsilon^{total}_0 = \sum_{k=1}^{K}$ | Phenomenological | 1 |

**Table 6 continued from previous page**

| Variables | Equations | Classification | Number of equation(s) |
|---|---|---|---|
| Total gas volume in the pulp phase | $V_{gas} = \sum_{k=1}^{K} V_{gas}^{k}$ | Phenomenological | 1 |
| Total upward gas velocity | $v_{g,\text{out pulp}}^{\text{total}} = \sum_{k=1}^{K} v_{g,\text{out pulp}}^{k} \varepsilon_0^k$ | Semi-empirical | 1 |
| Upward gas velocity | $v_{g,\text{out pulp}}^{k} = \frac{g\rho_{\text{pulp}}(d_{b,pulp}^{k})^2}{18\mu_{\text{pulp}}\left(1-\varepsilon_0^k\right)^{1.39}}$ | Semi-empirical | $K$ |
| Volumetric fraction of solids | $\phi = \frac{\rho_{\text{water}}}{\rho_{\text{water}}-\rho_{\text{solids}}+\frac{\rho_{\text{solids}}}{\Phi_{solids}}}$ | Phenomenological | 1 |
| | *Pulp-froth interface* | | |
| Interfacial bubble size | $d_{b,int} = \frac{\sum_{k=1}^{K} v_{gas,\text{out pulp}}^{k} \varepsilon_0^k}{\sum_{k=1}^{K} \frac{v_{gas,\text{out pulp}}^{k} \varepsilon_0^k}{d_{b,pulp}^{k}}}$ | Phenomenological | 1 |
| Interfacial gas velocity | $v_g^* = \frac{dh_p}{dt} + v_{g,\text{ out pulp}}^{\text{total}}$ | Phenomenological | 1 |
| | *Froth phase* | | |
| Air recovery | $\alpha = \frac{v_f l_{lip} h_{over}}{Q_{air,in}}$ | Phenomenological | 1 |
| Air recovery as a function of busting rate | $\alpha^* = \frac{v_g^* - v_b}{v_g^*}$ | Phenomenological | 1 |
| Axial dispersion | $D_{\text{axial}} = \frac{j_g^{1.5}}{\sqrt{k_1\left(\sqrt{3}-\frac{\pi}{2}\right)Pe}}$ | Phenomenological | 1 |
| Bubble surface area flux | $S_b = \frac{6v_g^*}{d_{b,int}}$ | Phenomenological | 1 |
| Bursting rate | $v_b = a + bj_g + cj_g^2$ | Semi-empirical | 1 |
| Concentrate flowrate | $Q_{conc} = \begin{cases} \frac{A_{cell} v_g^{*2} \lambda_{out}(1-\alpha^*)\alpha^*}{k_1} & \text{if } \alpha < 0.5 \\ \frac{A_{cell} v_g^{*2} \lambda_{out}}{4k_1} & \text{if } \alpha \geq 0.5 \end{cases}$ | Phenomenological | 1 |
| Entrainment factor | $ENT_i \approx \begin{cases} \exp\left(\frac{-v_{set,i}^{1.5} h_f}{D_{axial}\sqrt{v_g^*(1-\alpha^*)}}\right) & \text{if } \alpha < 0.5 \\ \exp\left(\frac{-2v_{\text{set},i}^{1.5} h_f}{D_{\text{axial}}\sqrt{v_g^*}}\right) & \text{if } \alpha \geq 0.5 \end{cases}$ | Phenomenological | $i$ |
| Froth height | $h_f = h_T - h_p$ | Phenomenological | 1 |
| Froth recovery | $R_{F,i} = \begin{cases} \left(\frac{\alpha^*(1-\alpha^*)v_g^*}{v_{\text{set},i}}\right)^{\frac{f}{2}} \left(\frac{d_{b,\text{ int}}}{d_{\text{bfroth}}}\right)^f & \text{if } \alpha < 0.5 \\ \left(\frac{v_g^*}{v_{\text{set},i}}\right)^{\frac{f}{2}} \left(\frac{d_{b,\text{ int}}}{d_{\text{bfroth}}}\right)^f & \text{if } \alpha \geq 0.5 \end{cases}$ | Phenomenological | $i$ |
| Froth residence time | $\tau_f = \frac{h_f}{v_g^*}$ | Phenomenological | 1 |

**Table 6 continued from previous page**

| Variables | Equations | Classification | Number of equation(s) |
|---|---|---|---|
| Length Plateau border out of the froth per volume | $\lambda_{out} = \frac{k_\lambda}{d^2_{b\text{froth out}}}$ | Phenomenological | 1 |
| Overflowing froth bubble size | $ODE : \frac{d}{dt} d_{b,froth} = C d^{1-n}_{b,froth}$<br>$Analyticalsolution : d_{b\text{froth out}} = \left( nC\tau_f + d^n_{b,int} \right)^{1/n}$ | Phenomenological | 1 |
| Overflowing froth velocity | $v_f = \frac{Q_{\text{concentrate}}}{\epsilon l_{\text{lip}}\, h_{\text{over}}}$ | Phenomenological | 1 |
| Physical constant | $k_1 = \frac{\rho_{\text{pulp}} g}{3 C_{PB} \mu_{\text{pulp}}}$ | Phenomenological | 1 |
| Settling velocity | $v_{set,i} = \frac{g(\rho_{\text{solid},i} - \rho_{\text{water}}) d^2_{p,i}}{18\mu_{\text{pulp}}} \frac{(1-\phi)^{4.65}}{3}$ | Phenomenological | $i$ |
| Slurry content | $\epsilon \approx \begin{cases} \frac{v^*_g}{k_1}(1-\alpha^*)\,\lambda_{out} \text{ if } \alpha < 0.5 \\ \frac{v^*_g}{2k_1}\lambda_{\text{out}} \text{ if } \alpha \geq 0.5 \end{cases}$ | Phenomenological | 1 |
| Solid mass flowrate in the concentrate due to entrainment | $m_{i,ENT} = Q_{\text{conc}} ENT_i C_{\text{tailings},i}$ | Phenomenological | $i$ |
| Solid mass flowrate in the concentrate due to true flotation | $m_{i,\text{true flotation}} = V_{\text{cell}} k_i R_{f,i} C_{\text{tailings},i}$ | Phenomenological | $i$ |
| Specific rate constant | $k_i = P_i S_b$ | Phenomenological | $i$ |
| | | **Total number of equations:** | $26{+}10i{+}5K$ |

## 6. Acknowledgements

Paulina Quintanilla would like to acknowledge the National Agency for Research and Development (ANID) for funding this research with a scholarship from "Becas Chile". The Society of Chemical Industry is also greatly acknowledged for the support granted by the SCI Messel Scholarship 2020.

## References

Ata, S., 2012. Phenomena in the froth phase of flotation - A review. International Journal of Mineral Processing 102-103, 1–12. URL: http://dx.doi.org/10.1016/j.minpro.2011.09.008, doi:10.1016/j.minpro.2011.09.008.

Bascur, O.A., 1982. Modelling and computer control of a flotation cell. University of Utah, Salt Lake City .

Bergh, L.G., Yianatos, J.B., 2011. The long way toward multivariate predictive control of flotation processes. Journal of Process Control 21, 226–234. doi:10.1016/j.jprocont.2010.11.001.

Bouchard, J., Desbiens, A., del Villar, R., Nunez, E., 2009. Column flotation simulation and control: An overview. Minerals Engineering 22, 519–529. URL: http://dx.doi.org/10.1016/j.mineng.2009.02.004, doi:10.1016/j.mineng.2009.02.004.

Chen, F., Gomez, C.O., Finch, J.A., 2001. Technical note bubble size measurement in flotation machines. Minerals Engineering 14, 427–432. doi:10.1016/S0892-6875(01)00023-1.

Chipili, C., Bhondayi, C., 2021. The role of the pulp-froth interface on particle detachment and selectivity. doi:10.1016/j.cis.2020.102296.

Coulson, J., Richardson, J., 1993. Chemical Engineering. Pergamon, Oxford, UK. doi:https://doi.org/10.1016/C2009-0-11215-1.

Desbiens, A., Hodouin, D., Mailloux, M., 1998. Nonlinear Predictive Control of a Rougher Flotation Unit Using Local Models. IFAC Proceedings Volumes 31, 287–292. URL: http://dx.doi.org/10.1016/S1474-6670(17)35893-7, doi:10.1016/S1474-6670(17)35893-7.

Desbiens, A., Hodouin, D., Najim, K.I., Flament, F., Universitaire, C., Gk, C., 1994. Long-range predictive control of a rougher flotation unit. Minerals Engineering 7, 21–37.

Dinariev, O.Y., Evseev, N.V., 2018. Modelling of flotation processes by density functional hydrodynamics. Minerals Engineering doi:10.1016/j.mineng.2018.06.013.

Ferreira, J.P., Loveday, B.K., 2000. Improved model for simulation of flotation circuits. Minerals Engineering doi:10.1016/S0892-6875(00)00129-1.

Feteris, S.M., Frew, J.A., Jowett, A., 1987. Modelling the effect of froth depth in flotation. International Journal of Mineral Processing 20, 121–135. doi:10.1016/0301-7516(87)90021-4.

Finch, J.A., Dobby, G.S., 1991. Column flotation: A selected review. Part I. International Journal of Mineral Processing doi:10.1016/0301-7516(91)90062-N.

Gharai, M., Venugopal, R., 2016. Modeling of flotation process - An overview of different approaches. Mineral Processing and Extractive Metallurgy Review 37, 120–133. doi:10.1080/08827508.2015.1115991.

Grau, R.A., Heiskanen, K., 2002. Visual technique for measuring bubble size in flotation machines. Minerals Engineering 15, 507–513. doi:10.1016/S0892-6875(02)00074-2.

Hadler, K., Cilliers, J.J., 2009. The relationship between the peak in air recovery and flotation bank performance. Minerals Engineering doi:10.1016/j.mineng.2008.12.004.

Hadler, K., Greyling, M., Plint, N., Cilliers, J.J., 2012. The effect of froth depth on air recovery and flotation performance. Minerals Engineering 36-38, 248–253. URL: http://dx.doi.org/10.1016/j.mineng.2012.04.003, doi:10.1016/j.mineng.2012.04.003.

Hadler, K., Smith, C.D., Cilliers, J.J., 2010. Recovery vs. mass pull: The link to air recovery. Minerals Engineering 23, 994–1002. URL: http://dx.doi.org/10.1016/j.mineng.2010.04.007, doi:10.1016/j.mineng.2010.04.007.

Herbst, J.A., Flintoff, B., 2012. Recent Advances in Modeling, Simulation, and Control of Mineral Processing Operations, in: Separation Technologies for Minerals, Coal, and Earth Resources, pp. 667–680.

Herbst, J.A., Harris, M., 2007. Modeling and Simulation of Industrial Flotation Processes, in: Froth Flotation: A Century of Innovation, pp. 757–777.

Hu, W., Hadler, K., Neethling, S.J., Cilliers, J.J., 2013. Determining flotation circuit layout using genetic algorithms with pulp and froth models. Chemical Engineering Science 102, 32–41. doi:10.1016/j.ces.2013.07.045.

Ityokumbul, M.T., Salama, A.I., Al Taweel, A.M., 1995. Estimation of bubble size in flotation columns. Minerals Engineering doi:10.1016/0892-6875(94)00104-K.

Jovanović, I., Miljanović, I., 2015. Contemporary advanced control techniques for flotation plants with mechanical flotation cells - A review. Minerals Engineering 70, 228–249. doi:10.1016/j.mineng.2014.09.022.

Jovanović, I., Miljanović, I., Jovanović, T., 2015. Soft computing-based modeling of flotation processes âĂŞ A review. Minerals Engineering 84, 34–63. doi:10.1016/J.MINENG.2015.09.020.

Lee, H.T., Neethling, S.J., Cilliers, J.J., 2005. Particle and liquid dispersion in foams. Colloids and Surfaces A: Physicochemical and Engineering Aspects 263, 320–329. doi:10.1016/j.colsurfa.2004.12.064.

Maldonado, M., Desbiens, A., Del Villar, R., Quispe, R., 2007. Towards the optimization of flotation columns using predictive control. IFAC Proceedings Volumes (IFAC-PapersOnline) 12, 75–80. doi:10.3182/20070821-3-CA-2919.00011.

Mesa, D., Brito-Parada, P.R., 2020. Bubble size distribution in aerated stirred tanks: Quantifying the effect of impeller-stator design. Chemical Engineering Research and Design 160, 356–369. doi:10.1016/j.cherd.2020.05.029.

Morrison, A., Brito-Parada, P., Cilliers, J., 2017. Tank design modifications for the improved performance of froth flotation equipment. Imperial College London .

Neethling, S., Cilliers, J., 2009. The entrainment factor in froth flotation: Model for particle size and other operating parameter effects. International Journal of Mineral Processing 93, 141–148. doi:10.1016/J.MINPRO.2009.07.004.

Neethling, S.J., Brito-Parada, P.R., 2018. Predicting flotation behaviour âĂŞ The interaction between froth stability and performance. Minerals Engineering 120, 60–65. URL: https://doi.org/10.1016/j.mineng.2018.02.002, doi:10.1016/j.mineng.2018.02.002.

Neethling, S.J., Cilliers, J.J., 2003. Modelling flotation froths. International Journal of Mineral Processing 72, 267–287. doi:10.1016/S0301-7516(03)00104-2.

Neethling, S.J., Cilliers, J.J., 2008. Predicting air recovery in flotation cells. Minerals Engineering 21, 937–943. doi:10.1016/j.mineng.2008.03.011.

Neethling, S.J., Lee, H.T., Cilliers, J.J., 2003. Simple relationships for predicting the recovery of liquid from flowing foams and froths. Minerals Engineering 16, 1123–1130. doi:10.1016/j.mineng.2003.06.014.

Oosthuizen, D.J., Craig, I.K., Jämsä-Jounela, S.L., Sun, B., 2017. On the current state of flotation modelling for process control. IFAC-PapersOnLine 50, 19–24. doi:10.1016/j.ifacol.2017.12.004.

Oosthuizen, D.J., le Roux, J.D., Craig, I.K., 2021. A dynamic flotation model to infer process characteristics from online measurements. Minerals Engineering 167, 106878. doi:10.1016/j.mineng.2021.106878.

Prakash, R., Majumder, S.K., Singh, A., 2018. Flotation technique: Its mechanisms and design parameters. Chemical Engineering and Processing - Process Intensification 127, 249–270. doi:10.1016/j.cep.2018.03.029.

Putz, E., Cipriano, A., 2015. Hybrid model predictive control for flotation plants. Minerals Engineering 70, 26–35. doi:10.1016/j.mineng.2014.08.013.

Quintanilla, P., Neethling, S.J., Brito-Parada, P.R., 2021. Modelling for froth flotation control: A review. Minerals Engineering 162, 106718. doi:10.1016/j.mineng.2020.106718.

Rodríguez, M., Gayoso, J.A., 2006. Degrees of freedom analysis for process control. Computer Aided Chemical Engineering 21, 1489–1494. doi:10.1016/S1570-7946(06)80258-0.

Alves dos Santos, N., Savassi, O., Peres, A.E.C., Martins, A.H., 2014. Modelling flotation with a flexible approach âĂŞ Integrating different models to the compartment model. Minerals Engineering 66-68, 68–76. URL: https://www.sciencedirect.com/science/article/pii/S0892687514001769, doi:10.1016/J.MINENG.2014.05.007.

Sbarbaro, D., del Villar, R., 2010. Advanced control and supervision for mineral processing. Advances in Industrial Control. doi:10.1007/978-1-84996-106-6.

Shean, B., Hadler, K., Cilliers, J.J., 2017. A flotation control system to optimise performance using peak air recovery. Chemical Engineering Research and Design 117, 57–65. doi:10.1016/j.cherd.2016.10.021.

Shean, B., Hadler, K., Neethling, S., Cilliers, J.J., 2018. A dynamic model for level prediction in aerated tanks. Minerals Engineering 125, 140–149. doi:10.1016/j.mineng.2018.05.030.

Shean, B.J., Cilliers, J.J., 2011. A review of froth flotation control. International Journal of Mineral Processing 100, 57–71. doi:10.1016/j.minpro.2011.05.002.

Tian, Y., Azhin, M., Luan, X., Liu, F., Dubljevic, S., 2018. Three-Phases Dynamic Modelling of Column Flotation Process. IFAC Proceedings Volumes 51, 99–104. doi:10.1016/j.ifacol.2018.09.399.

Tucker, J.P., Deglon, D.A., Franzidis, J.P., Harris, M.C., O'Connor, C.T., 1994. An evaluation of a direct method of bubble size distribution measurement in a laboratory batch flotation cell. Minerals Engineering 7, 667–680. doi:10.1016/0892-6875(94)90098-1.

Varbanov, R., Forssberg, E., Hallin, M., 1993. On the modelling of the flotation process. International Journal of Mineral Processing 37, 27–43. doi:10.1016/0301-7516(93)90003-S.

Wang, G., Ge, L., Mitra, S., Evans, G.M., Joshi, J.B., Chen, S., 2018. A review of CFD modelling studies on the flotation process. doi:10.1016/j.mineng.2018.08.019.

Wang, L., Peng, Y., Runge, K., Bradshaw, D., 2015. A review of entrainment: Mechanisms, contributing factors and modelling in flotation. doi:10.1016/j.mineng.2014.09.003.

Wang, Y., Neethling, S.J., 2006. Simulating realistic froth surfaces 19, 1069–1076. doi:10.1016/j.mineng.2006.03.007.

Zaragoza, R., Herbst, J.A., 1989. Model-based feedforward control scheme for flotation plants. Minerals and metallurgical processing , 177–185.